Shale oil potential of lacustrine black shale in the Eocene Dongying depression: Implications for geochemistry and reservoir characteristics

Chao Liang, Yingchang Cao, Zaixing Jiang, Jing Wu, Song Guoqi, and Yongshi Wang

ABSTRACT

The geochemistry and reservoir characteristics of the lacustrine shale in the Eocene Dongying depression are described in detail based on thin-section and field-emission–scanning electron microscope observations of well cores combined with x-ray diffraction, physical property testing, and geochemical indicators. The Eocene Shahejie (Es) Formation Es4s–Es3x shale member is predominantly carbonate, clay minerals, and quartz. Six lithofacies were identified: (1) laminated limestone (organic-rich laminated limestone and organic-poor laminated limestone), (2) laminated marl, (3) laminated calcareous mudstone, (4) laminated dolomite mudstone, (5) laminated gypsum mudstone, and (6) massive mudstone. The Es4s–Es3x shale samples from three cored wells had total organic carbon (TOC) contents in the range of 0.58 to 11.4 wt. %, with an average of 3.17 wt. %. The hydrocarbon generation potential (free hydrocarbons [S1] + the hydrocarbons cracked from kerogen [S2]) values range from 2.53 to 87.68 mg/g, with an average of 24.19 mg/g. The Es4s–Es3x shale of the Dongying depression has a high organic-matter content with very good or excellent hydrocarbon generation potential. The organic maceral composition is predominantly sapropelinite (up to 95%). The hydrogen index (being S2/TOC) versus the maximum yield temperature of pyrolysate (T_{max}) indicates that the organic matter is predominantly type I kerogen, which contains a high proportion of convertible organic carbon. The Es4s–Es3x shale is thermally mature and within the oil window, with the vitrinite reflectance values ranging from 0.46% to 0.74% and the T_{max}

Manuscript received December 26, 2015; provisional acceptance May 3, 2016; revised manuscript received July 6, 2016; revised manuscript provisional acceptance November 7, 2016; 2nd revised manuscript received November 14, 2016; final acceptance January 25, 2017.
DOI:10.1306/01251715249

AUTHORS

CHAO LIANG ~ *Laboratory for Marine Mineral Resource, Qingdao National Laboratory for Marine Science and Technology, Qingdao 266071, China; present address: School of Geosciences, China University of Petroleum, No. 66, Changjiang West Road, Huangdao District, Qingdao 266580; liangchao0318@163.com*

Chao Liang is currently a postdoctoral scholar of sedimentary geology at China University of Petroleum. He received his Ph.D. from China University of Geosciences (Beijing) in 2015. His research focuses on shale sedimentology, sequence stratigraphy, shale diagenesis, and shale reservoir quality prediction.

YINGCHANG CAO ~ *School of Geosciences, China University of Petroleum, No. 66, Changjiang West Road, Huangdao District, Qingdao 266580, China; caoych@upc.edu.cn*

Yingchang Cao is a professor at China University of Petroleum. His research interests lie in the fields of sequence stratigraphy, sedimentology, and sandstone reservoir quality prediction.

ZAIXING JIANG ~ *School of Energy Resource, China University of Geosciences, No. 29, Xueyuan Road, Haidian District, Beijing 100083, China; jiangzx@cugb.edu.cn*

Zaixing Jiang is a professor of sedimentary geology at the China University of Geosciences (Beijing). He received his Ph.D. from the Graduate School of the Chinese Academy of Sciences in 1997. He is currently leading a group working on hydrocarbon sedimentology and sequence stratigraphy.

JING WU ~ *Exploration and Production Research Institute, Sinopec, No. 30, Xueyuan Road, Haidian District, Beijing 100083, China; wujing6524982@163.com*

Jing Wu is currently a postdoctoral scholar of sedimentary geology at the Exploration and Production Research Institute. She received her Ph.D. from China University of Geosciences (Beijing) in 2015. Her research focuses on shale sedimentology and sequence stratigraphy.

SONG GUOQI ~ *Geological Scientific Research Institute, Sinopec Shengli Oilfield, No. 2, Liaocheng Road, Dongying 257015, China; songguoqi.slyt@sinopec.com*

Guoqi Song received his Ph.D. from the Geology and Geophysics Institute of the Chinese Academy of Sciences. He is currently the chief exploration expert at Shengli Oilfield Company, Sinopec. He has been involved in the investigation and study of petroleum exploration of Chinese terrestrial fault basins since 1982. His research focuses on sequence stratigraphy, sedimentology, and petroleum systems of fault basins.

YONGSHI WANG ~ *Geological Scientific Research Institute, Sinopec Shengli Oilfield, No. 2, Liaocheng Road, Dongying 257015, China; wangysh623@sina.com*

Yongshi Wang received his Ph.D. from China University of Mining and Technology. He is currently the exploration expert at Shengli Oilfield Company, Sinopec. His research focuses on sequence stratigraphy, sedimentology, and petroleum systems of fault basins.

ACKNOWLEDGMENTS

The work presented in this paper was supported by the Certificate of China Postdoctoral Science Foundation Grant (2015M582165), National Natural Science Foundation of China (41602142, U1262203, 41372107), and Natural Science Foundation of Shandong Province (ZR2016DB16). We are grateful to the Geoscience Institute of the Shengli Oilfield, Sinopec, for permission to access their in-house database. Our deepest gratitude goes to AAPG Editor Barry J. Katz and reviewers Wayne Camp and Dario De Benedictis for their careful work and thoughtful suggestions that have helped improve this paper substantially.

EDITOR'S NOTE

Color versions of Figures 1–10 and 12 can be seen in the online version of this paper.

value ranging from 413°C to 450°C, with the average being 442°C. The shale contains interparticle pores, organic-matter pores, dissolution pores, intracrystalline pores, interlaminar fractures, tectonic fractures, and abnormal-pressure fractures. The primary matrix pore storage is secondary recrystallized intercrystal pores and dissolution pores that formed during thermal maturation of organic matter. The TOC content and effective thickness of the organic-rich shales are the primary factors for hydrocarbon generation. The reservoir capacity is related to the scale, abundance, and connectivity of pore spaces, which are controlled by the characteristics of the lithofacies, mineral composition, TOC content, and microfractures.

INTRODUCTION

Shale oil and gas is an unconventional petroleum system in which the shale is both the source and reservoir, which is derived from the organic matter within the shale via biogenic and/or thermogenic processes (Hill et al., 2007; Jarvie et al., 2007; Hao et al., 2013). For shale oil and gas plays, a large number of studies focus on marine shale, including marine siliciclastic shale, such as the Mississippian Barnett Shale in the Fort Worth Basin and Mississippian Bakken Formation in Williston Basin, and marine calcareous shale, such as Upper Cretaceous Eagle Ford shale in Western Gulf Basin and Upper Cretaceous Niobrara member of the Mancos Shale in the San Juan Basin (Loucks and Ruppel, 2007; Abouelresh and Slatt, 2012; Kuhn et al., 2012; El Attar and Pranter, 2016; Fairbanks et al., 2016). All these shales have commercial shale oil or gas. With the successful exploration and development of marine shale oil and gas, the lacustrine shale gradually becomes the focus of attention. The studies on lacustrine shale have been carried out in the Green River Formation, Uinta Basin; Brown Shale in the Sumatra Basin; and other Southeast Asia Mesozoic and Cenozoic lacustrine rift basins (Schenk et al., 2010; Burton et al., 2014; Schenk et al., 2015). Generally, studies on lacustrine shales, particularly carbonate-rich (~50% carbonate) shale, are relative sparse (Bai et al., 2009; Jia et al., 2013; Wang et al., 2013).

Lacustrine shales are widely present in the Mesozoic and Cenozoic terrestrial lacustrine strata of East China and have vastly different mineral components than marine shale (Liu et al., 2001; Jiang, 2011; Jiang et al., 2013; Wang et al., 2013). In recent years, because of the increasing demand for unconventional oil and gas exploration, especially for shale oil and gas in China (Wang et al., 2013; Zou et al., 2013), the Sinopec Shengli oilfield conducted research on lacustrine-shale oil exploration in the Dongying depression of the Bohai Bay Basin. The study interval was the Paleogene Shahejie (Es) Formation Es4s–Es3x shale, which is

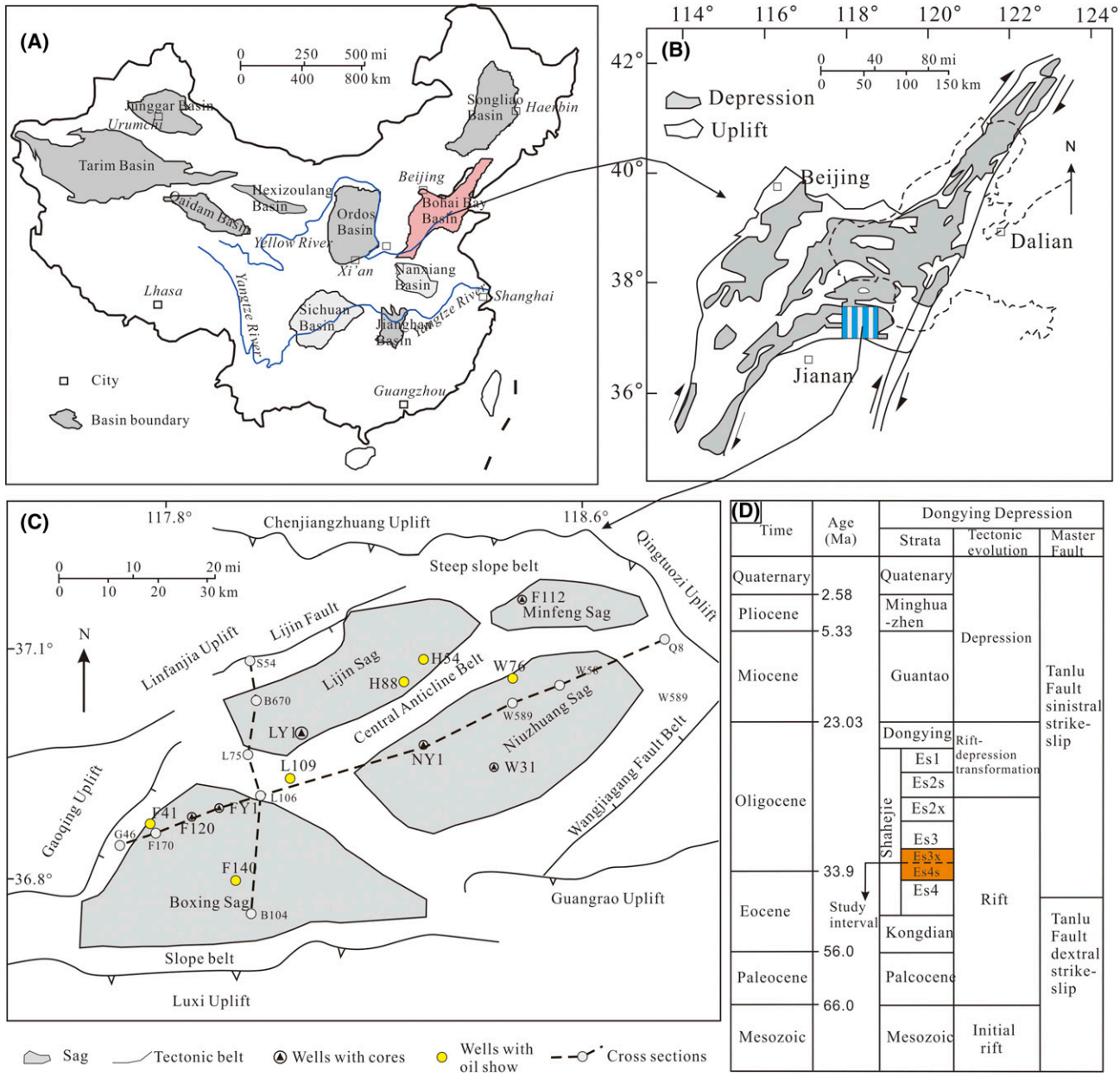

Figure 1. Regional index map showing the study area. (A) The location of Bohai Bay Basin in China. (B) The location of Dongying depression in the Bohai Bay Basin. (C) Tectonic features mapped on the top of the Shahejie Formation Es3x interval of Dongying depression and the locations of key wells. (D) Stratigraphic column of the study area.

predominantly carbonate and clay minerals with a carbonate content of up to 80 wt. %. Currently, several wells have commercial oil flow, which fully demonstrates the great potential for shale oil exploration (Lu et al., 2012; Song et al., 2013). Understanding the characteristics of shale facilitates the analysis of the lacustrine-shale oil exploration potential and the contrasts of marine and lacustrine-shale reservoir characteristics.

GEOLOGICAL SETTING

The Dongying depression is located in the southeastern part of the Bohai Bay Basin in East China (Figure 1A). It is 5700 km^2 (2200 mi^2) in area and bordered by the Tuoshengyong fault, Chenjiazhuang uplift, and Binxian uplift in the north; the Luxi uplift and Guangrao uplift in the south; the Linfanjia tectonic belt and Gaoqing uplift in the west; and the Qingtuozi

uplift in the east. The Dongying depression is composed of several secondary structural units, including the Lijin sag, Boxing sag, Niuzhuang sag, Minfeng sag, central anticline belt, north steep slope belt, and south slope belt.

The study area comprises Cenozoic rift basin strata that have local thicknesses of up to 5000 m (16,400 ft) in the depocenter, consisting of the Kongdian, Es, Dongying, Guantao, Minghuazhen, and Pingyuan Formations. The Es Formation is subdivided into four members from the top to base: Es1, Es2, Es3, and Es4. The basin started to expand after the Mesozoic. The Es4s–Es3x members are the main expansion period and the period in which the lake level reached a maximum (Qiu et al., 2006; Sheng et al., 2008; Xue et al., 2013). In this period, the Dongying depression was a semideep lake environment with the anoxic conditions at the bottom of the lake (Liu et al., 2004) that promoted preservation of organic matter. The warm and humid paleoclimate during this period promoted high levels of organic productivity (lacustrine algae) (Zhu et al., 2005; Wang, 2012). The combination of high organic productivity, anoxic conditions, and rift basin subsidence resulted in deposition up to 400 m (1312 ft) of organic-rich black shale in the upper Es4 member (Es4s) and lower Es3 member (Es3x), which is our study interval (Figure 1B).

PREVIOUS STUDIES

The Shengli oilfield proposed a series of projects on shale oil exploration in Dongying depression beginning in 2009. Studies show that Dongying depression has abundant shale oil resources in the Es4s–Es3x, with resources of 24×10^8 t (1.76×10^{10} bbl) (Wu et al., 2013). Currently, there are 110 wells that produce (or are capable of producing) oil and gas from the Es4s–Es3x shale in Dongying depression (Song et al., 2013; Wang et al., 2013). The oil saturation of the Es4s–Es3x shale ranges from 4.5% to 72%, and the formation reaches a maximum at 3700 m (12,150 ft) depth, which corresponds to the peak of hydrocarbon generation (Zhang et al., 2014). Studies suggest that the total movable oil can reach 9%–30% within the depth of 2800–4000 m (9200–13,100 ft) (Zhang et al., 2014; Li et al., 2016). Several wells have flowed oil at a commercial level (Table 1) with cumulative production of 10,000 t (73,500 bbl) through 2009, which fully demonstrates the great potential for shale oil exploration

Table 1. Well Information

Well	Interval	Oil Rate (t/day [b/day])	Gas Rate (m^3/day [ft^3/day])	Method	Lithology	TOC (wt. %)	Thickness (m [ft])
DF1	Es3x	24 (176.4)	nd	Acidification	Shale with interbedded siltstone	nd	47 (154)
F41	Es3x	4.49 (33)	nd	Swabbing	Oil shale, calcareous shale	7.2	21 (68.9)
F119	Es4s	15.9 (116.9)	1480 (52,266)	Flowing	Marl, sandy limestone	2.5	15 (49.2)
F120	Es4s	5.14 (37.8)	nd	Testing	Oil shale, marl and calcareous shale	4.89	25 (82)
F140	Es4s	21.1 (155.1)	nd	Testing	Oil shale with interbedded dolomite and siltstone	3.36	68 (223.1)
G7	Es4s	14.4 (105.8)	nd	Fracturing	Oil shale with interbedded dolomite	nd	54 (177.2)
H54	Es3x	91.3 (671.1)	2740 (96,762)	Flowing	Oil shale with interbedded siltstone	2.8	45 (147.6)
H88	Es4s	5.89 (43.3)	nd	Swabbing	Calcareous shale	3.2	12 (39.4)
L758	Es3x	5.81 (42.7)	nd	Swabbing	calcareous shale and marl	nd	62 (203.4)
S13	Es4s–Es3x	12.1 (88.9)	nd	Testing	calcareous shale and marl	4.63	180 (590.6)
W76	Es4s	21.5 (158)	nd	Testing	Oil shale, calcareous shale	3.1	78 (255.9)
XLS1	Es4s	99.9 (734.3)	25,448 (898,689)	Testing	Oil shale with interbedded siltstone	nd	125 (410.1)
Y20	Es3x	8.9 (65.4)	nd	Testing	Oil shale with interbedded dolomite	3.87	91 (298.6)
Y54	Es3x	46.5 (341.8)	nd	Testing	Calcareous shale with interbedded siltstone	5.57	188 (616.8)

See well locations in Figure 1A. Data from Wang et al. (2013).
Abbreviations: Es = Shahejie Formation; nd = no data available; TOC = total organic carbon.

(Lu et al., 2012; Wu et al., 2013; Chen et al., 2015). These commercial oil wells are mostly vertical, with partial acidification or artificial fracturing (Table 1). The Es4s–Es3x unit is overpressured at 2800–4000 m (9200–13,100 ft) (Zhang et al., 2009; He et al., 2012), with the formation pressure coefficient ranging from 1.5 to 1.7 (Liu et al., 2012; Li et al., 2015; Nie et al., 2016). The formation pressure coefficient refers to the ratio of actual pore pressure to hydrostatic pressure at the same depth, and the value greater than 1 indicates overpressure (Guo et al., 2016). The oil is characterized by a low gas–oil ratio and a high wax content, ranging from 17.24% to 21.54% (Zhang et al., 2014; Saraji and Piri, 2015; Li et al., 2016).

DATA AND METHODS

The basic data include a total of 800 m (2600 ft) of core and 816 thin sections from 3 wells (NY1, LY1, and FY1, Figure 1A), 48 field-emission–scanning electron microscope (FESEM) samples, well logs and oil production from 106 wells, rock pyrolysis analysis, maceral composition and organic carbon data from 300 samples, and x-ray diffraction data from 300 samples.

The thin-section observations were taken using a Zeiss microscope Axio Scope A1, and samples were prepared with a thickness of 0.03 mm. The mineral x-ray diffraction was performed using a D/max-2500 theta/theta rotating anode x-ray diffractometer. Prior to analysis, each sample was oven dried at 40°C for 2 days and ground to less than 40 mm using an agate mortar to thoroughly disperse the minerals. Computer analysis of the diffractograms enabled the identification and semiquantitative analysis of the relative abundance (in weight percent) of the various mineral phases. The organic carbon content was determined using a Leco carbon–sulfur analyzer CS600 and gas-shows evaluation instrument. The test temperature was 27°C. The measurement technique is based on the combustion of the sample in an oxygen atmosphere to convert the total organic carbon (TOC) to CO_2 (Charles and Simmons, 1986). The asphalt extraction was done before pyrolysis, and the Rock-Eval parameters measured included the free hydrocarbons (S1), the hydrocarbons cracked from kerogen (S2), the carbon dioxide relieved from organic matter (S3), and the maximum yield temperature of pyrolysate (T_{max}) (Barker, 1974; Espitalie et al., 1986). Ar-ion-beam milling, which provides flat surfaces for high-magnification imaging (Loucks et al., 2012), was used to prepare samples for imaging nanopores. High-resolution FESEM was used to observe minerals and micro- and nano-sized pores. The samples were gold coated and observed using a Hitachi S-4800 FESEM with a working current set at 10 kV. The porosity and permeability were measured using Boyle's law instruments of an Ultrapore-200A He porosimeter and Ultra-perm TM200 permeameter. These measurements were performed under room temperature conditions at 25°C, with humidity at 40%.

MINERALOGY

The Es4s–Es3x shale predominately consists of carbonate minerals, clay minerals, and quartz, with subordinate plagioclase, potassium feldspar, and pyrite (Tables 2, 3). Calcite is the dominant mineral (Figure 2), ranging from 1 to 79 wt. %, with an average of 37.8 wt. %, and dolomite content ranges from 1 to 56 wt. %, with an average of 13.1 wt. %. The carbonate is mostly clay- to silt-sized crystalline calcite (Figure 3A) and dolomite, with a small amount of calcareous biological debris, such as ostracod fragments and calcispheres (Figure 3B). The clay minerals range from 2 to 53 wt. %, with an average of 21.2 wt. %. Clay minerals are dominantly illite and illite–smectite mixed layer minerals. The relative content of illite is 41–100 wt. % (average: 85.3 wt. %), and the illite–smectite mixed layer is 1–57 wt. % (average: 15.2 wt. %). Quartz is also common, with a content ranging from 2 to 39 wt. % and an average of 21.9 wt. %. The quartz is clay–silt size and is in two forms: terrigenous clastic particles, found in the massive and laminated silty shale, with a particle size of tens of microns, and microcrystalline quartz, which is smaller than 10 μm and surrounded by clay minerals (Figure 3C). The plagioclase content ranges from 1 to 17 wt. %, with an average of 5.8 wt. %. The pyrite content ranges from 1 to 10 wt. %, with an average of 3.1 wt. %, which mostly occurs as framboidal pyrite, with a size of 5–20 μm, surrounded by clay minerals (Figure 3D).

Table 2. The TOC Content, Pyrolysis Parameters, and Mineral Content (wt. %) of the Es4s–Es3x Shale in Well NY1

Sample	TOC/wt. %	S1 (mg/g)	S2 (mg/g)	S1 + S2 (mg/g)	T_{max} (°C [°F])	Bitumen "A"	Clay Fraction (%)		Mineral Content (wt. %)					
							I/S	I	Total Clay	Qtz	Pl	Cal	Dol	Py
NY1-1	5.5	5.48	37.81	43.29	445 (833)	1.53	15	85	15	20	4	58	1	2
NY1-2	6.21	5.56	43.64	49.2	446 (834.8)	1.54	11	88	26	25	4	37	4	4
NY1-3	2.25	2.54	12.83	15.37	442 (827.6)	0.75	nd	nd	24	26	6	35	3	5
NY1-4	2.18	1.9	13.34	15.24	442 (827.6)	0.82	16	84	16	30	3	44	4	2
NY1-5	1.62	1.46	9.12	10.58	442 (827.6)	0.5	18	80	27	28	4	29	7	4
NY1-6	3.33	4.38	22.23	26.61	444 (831.2)	1.13	nd	nd	19	21	2	51	4	2
NY1-7	1.58	2.11	7.94	10.05	442 (827.6)	0.65	nd	nd	34	26	3	33	1	2
NY1-8	3.38	4.2	23.03	27.23	443 (829.4)	1.2	21	78	13	25	1	32	27	2
NY1-9	1.95	1.64	9.91	11.55	442 (827.6)	1.08	1	98	31	29	2	35	0	2
NY1-10	3.18	3.81	19.25	23.06	446 (834.8)	1.12	13	85	21	25	2	48	1	2
NY1-11	2.93	4.52	17.19	21.71	443 (829.4)	1.26	nd	nd	11	26	1	57	3	2
NY1-12	2.18	2.78	12.44	15.22	446 (834.8)	0.93	21	77	24	23	4	40	5	3
NY1-13	2.61	3.31	15.82	19.13	446 (834.8)	0.86	nd	nd	14	29	2	48	4	2
NY1-14	3.41	4.01	21.71	25.72	447 (836.6)	1.22	nd	nd	18	31	3	38	6	3
NY1-15	4.18	2.47	11.76	14.23	443 (829.4)	1.53	18	82	25	18	4	42	7	3
NY1-16	6.53	10.72	44.02	54.74	446 (834.8)	3.01	15	85	19	31	2	44	2	2
NY1-17	2.26	4.49	14.09	18.58	445 (833)	1.03	nd	nd	12	24	2	45	15	2
NY1-18	2.26	3.44	13.87	17.31	446 (834.8)	0.84	10	90	16	38	5	32	5	3
NY1-19	2.42	4.62	13.58	18.2	443 (829.4)	1.18	nd	nd	35	28	4	11	18	4
NY1-20	3.02	7.15	19.68	26.83	443 (829.4)	1.58	13	87	4	18	1	50	27	0
NY1-21	2.35	4.72	14.09	18.81	443 (829.4)	1.15	nd	nd	19	22	3	49	3	3
NY1-22	2.29	3.93	14.41	18.34	447 (836.6)	0.96	nd	nd	23	13	4	50	5	3
NY1-23	2.39	4.2	13.07	17.27	443 (829.4)	1.15	20	80	17	16	4	45	17	1
NY1-24	2.12	3.92	13.23	17.15	446 (834.8)	0.94	nd	nd	13	8	2	66	9	2
NY1-25	4.32	6.36	30.17	36.53	448 (838.4)	1.5	0	100	6	4	1	34	52	3
NY1-26	3.46	5.6	22.21	27.81	446 (834.8)	1.27	nd	nd	14	18	3	57	5	2
NY1-27	2.51	3.76	16.06	19.82	447 (836.6)	1.03	nd	nd	23	17	5	37	15	2
NY1-28	2.05	2.97	10.34	13.31	441 (825.8)	0.89	26	74	19	13	5	36	22	5
NY1-29	4.71	5.44	27.42	32.86	443 (829.4)	1.32	15	85	14	15	2	2	56	10
NY1-30	2.62	7.44	10.6	18.04	430 (806)	1.83	nd	nd	23	14	5	43	14	1
NY1-31	3.42	6.68	15.29	21.97	439 (822.2)	1.53	12	87	16	17	9	48	8	2
NY1-32	1.13	4.23	4.39	8.62	425 (797)	0.85	nd	nd	3	8	2	53	31	3
NY1-33	2.86	3.65	11.34	14.99	440 (824)	0.91	0	98	28	17	7	13	27	6
NY1-34	1.95	3.1	6.48	9.58	434 (813.2)	0.88	13	85	9	8	6	70	3	4
NY1-35	0.39	0.82	0.82	1.64	425 (797)	0.26	nd	nd	50	25	6	5	4	4
NY1-36	0.36	0.23	0.31	0.54	410 (770)	0.14	21	77	47	32	11	0	7	2
NY1-37	1.23	1.86	2.67	4.53	418 (784.4)	0.65	nd	nd	53	23	11	4	4	4
NY1-38	0.99	3.26	3.63	6.89	429 (804.2)	0.73	8	92	2	0	17	79	2	0
NY1-39	1.38	3.93	3.74	7.67	425 (797)	0.80	18	82	39	21	11	3	18	4
NY1-40	2.44	9.98	7.71	17.69	433 (811.4)	1.95	15	85	36	17	9	9	24	2

Because of space limitations, only the data of well NY1 are listed. The illite and I/S content indicate the clay mineral fraction.

Abbreviations: Cal = calcite; Dol = dolomite; Es = Shahejie Formation; I = illite; I/S = illite–smectite mixed layer; nd = no data available; Pl = plagioclase; Py = pyrite; Qtz = quartz; S1 = free hydrocarbons; S2 = hydrocarbons cracked from kerogen; T_{max} = maximum yield temperature of pyrolysate; TOC = total organic carbon.

Table 3. Average Mineral Content (wt. %) of the Es4s–Es3x Shale in the Dongying Depression

Well	Interval	Mineral Content (wt. %)						Clay Fraction (%)	
		Total Clay	Qtz	Cal	Dol	Pl	Py	Illite	I/S
NY1	3295–3500 m (10,810–11,483 ft)	22.1	18.9	35.7	13.1	6.6	3.0	83.5	15.4
FY1	3051–3451 m (10,010–11,322 ft)	21.1	24.1	37.5	10.0	4.1	3.1	87.5	11.2
LY1	3581–3700 m (11,749–12,139 ft)	28.8	24.5	30.7	6.9	4.6	3.2	77.3	19.7

The illite and illite–smectite mixed clayey (I/S) contents indicate the ratio in the clay mineral. Because of space limitations, only the average mineral content data of every well are listed.

Abbreviations: Cal = calcite; Dol = dolomite; Es = Shahejie Formation; Pl = plagioclase; Py = pyrite; Qtz = quartz.

LITHOFACIES

Laminated Limestone

Organic-Rich Laminated Limestone

Organic-rich laminated limestone (LL-1) is characterized by a high carbonate content (up to 80 wt. %) and high TOC content (4.0–9.8 wt. %), whereas clay minerals and terrigenous silts are rare (Table 4). The cores and thin sections show the clear laminar boundaries, and laminae have pure mineral components (Figure 4A). The light laminae are composed of recrystallization calcite, which occurs as "needles" or closely packed grain crystals (Figure 5A). The dark laminae are composed of clay minerals, organic matter, and pyrite.

Organic-Poor Laminated Limestone

Carbonate mineral content is greater than 50 wt. % (Table 4). Laminae are well developed and horizontal or wavy (Figure 4B). The light laminae are micritic calcite with subordinate quartz and feldspar, whereas the dark laminae consist of clay and organic matter. The organic laminae are thin, and the TOC content is relatively low: less than 2.0 wt. %. The cores and thin sections show that the calcite laminae are dominant in the organic-poor laminated limestone with relatively high thickness (Figure 5B). Some calcite laminae are lenticular (Figure 5B), suggesting the result of current deposition.

Laminated Marl

The calcite content is extremely high, with an average of 56 wt. %, whereas the content of terrigenous clastic (clay minerals and silt) is relatively low (Table 4). The TOC content ranges from 2.0 to 4.0 wt. %. Bright and dark laminae are interbedded, with clear boundaries between laminae observed in both hand specimens and microscopic sections (Figure 4C). Bright laminae are composed of micrite calcite, and dark laminae are clay minerals with organic matter. Typically, light laminae are thicker than dark laminae (Figure 5D). Sparry calcite locally occurs at the edge of micritic calcite laminae with large and clean crystals (Figure 5D) as a result of the recrystallization process.

Laminated Calcareous Mudstone

In hand specimens, laminated lime mudstone is grayish black or dark gray, with the calcium carbonate content ranging from 25 to 50 wt. %. The TOC content is 2.0–4.0 wt. % (Table 4). Laminae are 1–4 mm thick; dark laminae are thicker than bright laminae,

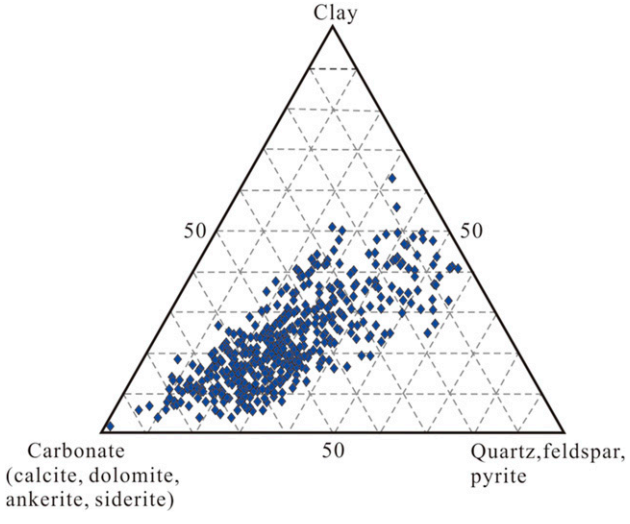

Figure 2. Ternary diagram of the mineral composition of the Shahejie Formation Es4s–Es3x shale.

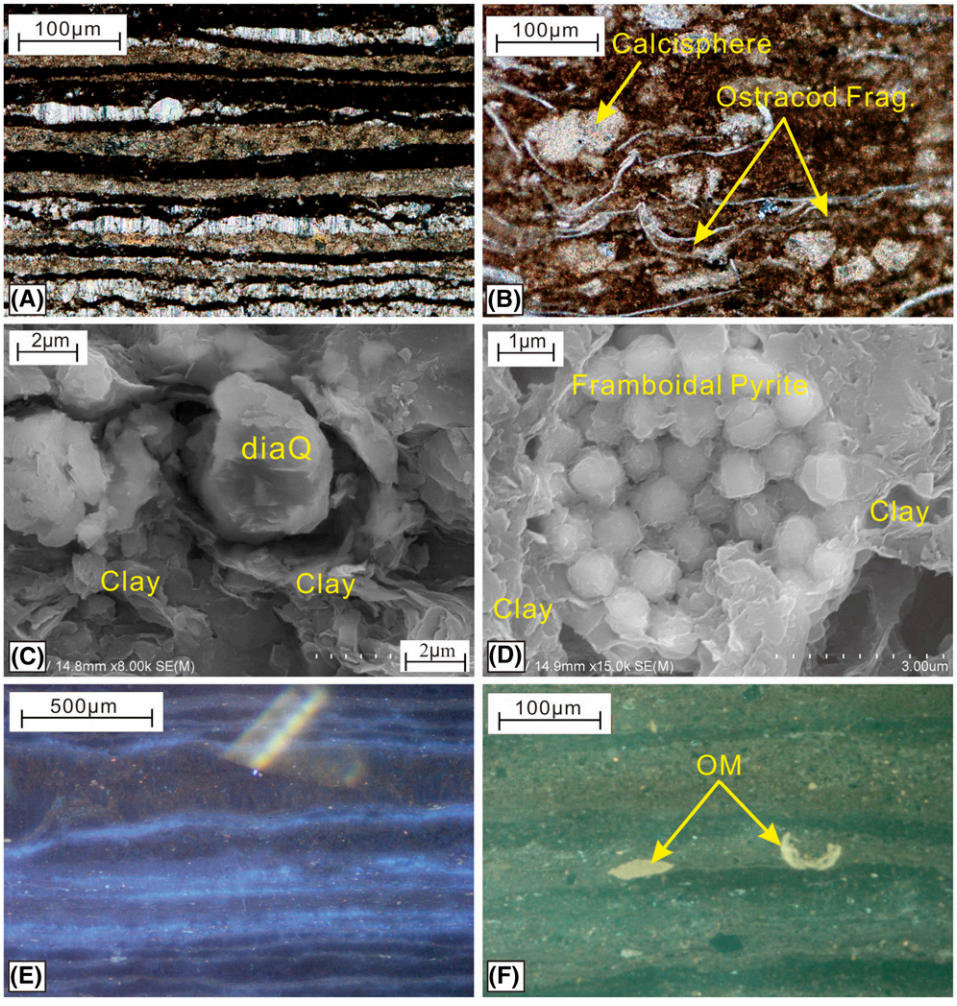

Figure 3. Mineral characteristics of the Formation Es4s–Es3x shale. (A), (B), (E), and (F) Thin-section images. (C) and (D) Secondary electron field-emission–scanning electron microscope (FESEM) images of non–Ar-ion-beam polished samples. (A) Cross-polarized light (CPL) view showing columnar and granular calcite crystals, well FY1, 3385.54 m (11,107.41 ft). (B) A CPL view showing calcareous biological debris in the limestone, well FY1, 3301.33 m (10,831.13 ft). (C) An FESEM view showing microquartz (diaQ) surrounded by clay minerals, grain size 4 μm, well FY1, 3308.4 m (10,854.33 ft). (D) An FESEM image showing framboidal pyrite surrounded by clay minerals, well NY1, 3402.3 m (11,162.40 ft). (E) Fluorescent organic-rich laminae, well FY1, 3325.49 m (10,910.4 ft). (F) Fluorescence image showing sporinite in the shale, NY1, 3437.2 m (11,276.90 ft). Frag. = Fragment; OM = organic matter.

which are composed of calcite (Figure 4D). Dark laminae are clay minerals with organic matter (Figure 5E).

Laminated Dolomite Mudstone

The laminated dolomite mudstone (LDM) is typically light-gray to gray colored in hand specimens. The dolomite content ranges from 25 to 50 wt. % (Table 4) and may occur as mud crystal, microcrystal, and sparry crystal, part of which is associated with rhombic automorphic crystals of anhydrite. The lithofacies is poor in organic matter, and the TOC content is less than 2.0 wt. %.

Laminated Gypsum Mudstone

The anhydrite content ranges from 20 to 50 wt. %, and most of the remaining materials are clay (Table 4). The anhydrite occurs as laminae or fragments, and anhydrite with swallowtail twins can be observed in the well cores (Figure 4E). This lithofacies is interpreted to have been deposited in an evaporation environment. This lithofacies develops at the lower Es4s.

Massive Mudstone

This lithofacies is gray or blue gray and massive in well cores (Figure 4F), locally developing indistinct horizontal bedding. Massive mudstone (MM) is overlain by laminated shale or siltstone, exhibiting a sharp contact at the base (Figure 4F). The mineral composition is clay minerals (~50 wt. %), calcite (ranging from 10 to 20 wt. %), and siliceous debris (ranging from 10 to 35 wt. %). In addition, a small amount of ostracod debris and oriented charcoal debris can be found (Figure 5F). The MM is poor in organic matter, with TOC content ranging from 0.4 to 0.8 wt. % (Table 4).

Table 4. Average Value of TOC Content, Mineral Composition, Porosity, and Permeability of Different Lithofacies

Lithofacies	TOC/wt. % Range (Average)	Mineral Composition (wt. %)					Porosity/%	Permeability/md
		Cal.	Dol.	An.	Qtz + Pl.	Total Clay		
LL-1	4.0–9.8 (4.68)	64.2	10.1	0	10.9	14.8	7%–10%	>1
LL-2	1.6–2.0 (1.87)	65.6	8.7	0	14.5	12.2	5%–6%	0.5–1
LM	2.0–4.0 (2.73)	56	8.2	0	19.3	18.4	6%–7%	>1
LCM	2.0–4.0 (2.56)	39.4	6.6	0	23.3	30.7	6%–8%	>1
LDM	0.8–1.9 (1.06)	5.9	31.8	18.2	10.5	33.6	4%–5%	<0.5
LGM	0.9–1.38 (1.22)	3.6	15.5	30.2	13.8	36.9	3%–5%	<0.5
MM	0.4–0.8 (0.67)	10.7	6.6	0	33.2	49.5	4%–5%	<0.5

Abbreviations: An. = anhydrite; Cal. = calcite; Dol. = dolomite; LCM = laminated calcareous mudstone; LDM = laminated dolomite mudstone; LGM = laminated gypsum mudstone; LL-1 = organic-rich laminated limestone; LL-2 = organic-poor laminated limestone; LM = laminated marl; MM = massive mudstone; Pl. = plagioclase; Qtz = quartz; TOC = total organic carbon.

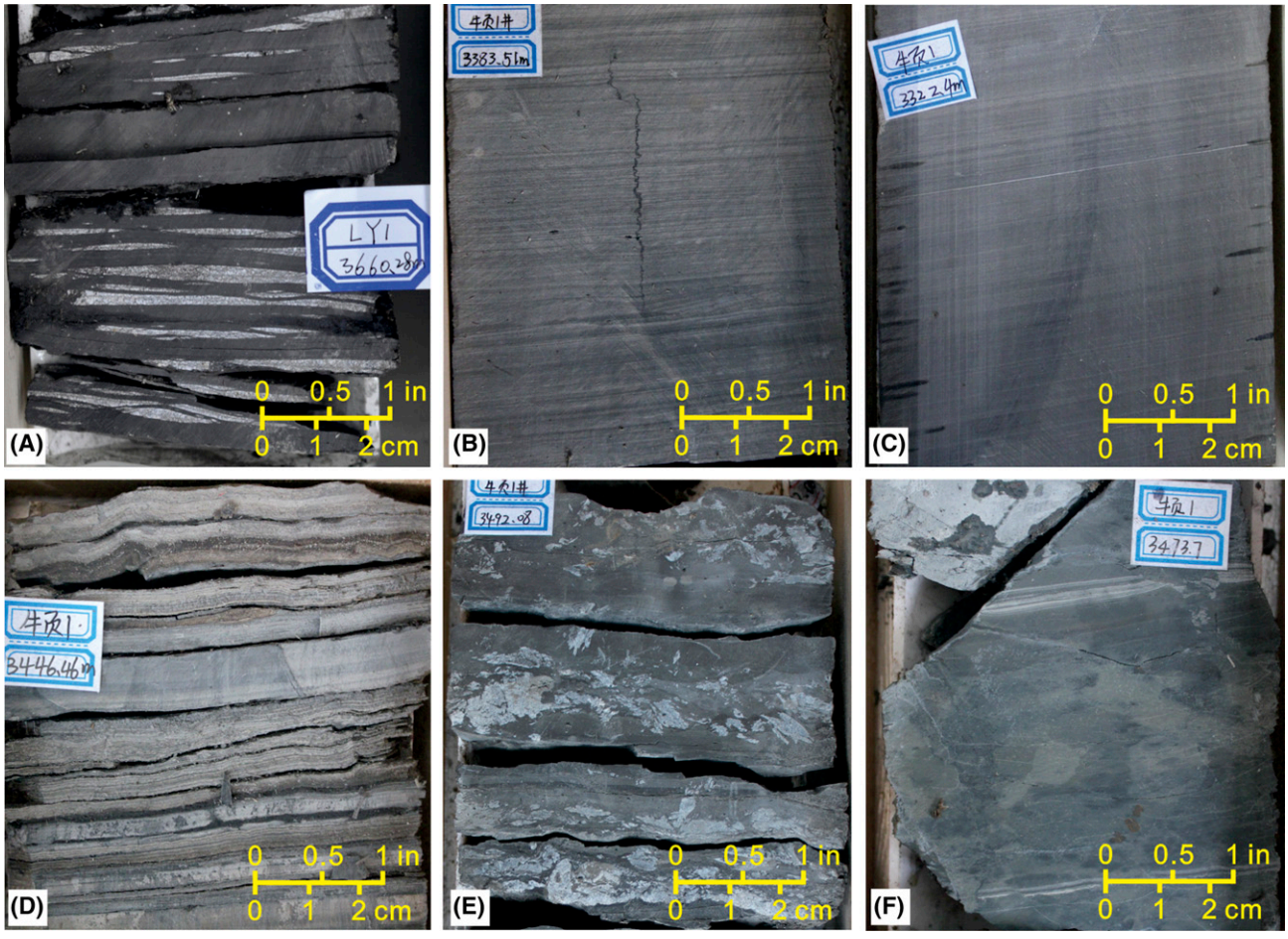

Figure 4. The macrocharacteristics of lithofacies. (A) Organic-rich laminated limestone with lenticular calcite, well LY1, 3660.28 m (12,008.79 ft). (B) Organic-poor laminated limestone, well NY1, 3383.51 m (11,100.75 ft). (C) Laminated marl, well NY1, 3322.4 m (10,900.26 ft). (D) Laminated calcareous mudstone, well NY1, 3446.46 m (11,307.28 ft). (E) Gypsum claystone with swallowtail twins in the anhydrite, well NY1, 3492.08 m (11,456.95 ft). (F) Gray massive mudstone, well NY1, 3473.7 m (11,396.65 ft).

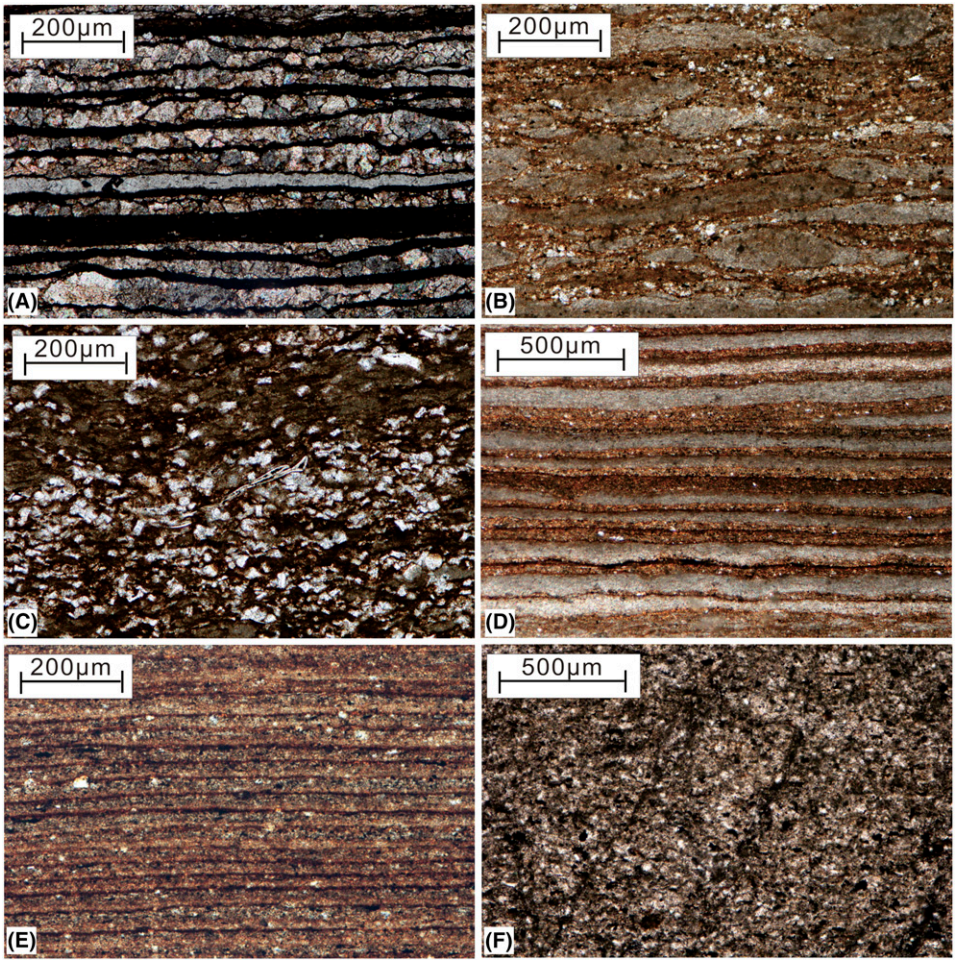

Figure 5. The thin-section images show microscopic characteristics of lithofacies. (A) Organic-rich laminated limestone with columnar and granular calcite crystals, well NY1, 3464.89 m (11,364.83 ft), plane-polarized light (PPL). (B) Organic-poor laminated limestone with lenticular micritic calcite, well NY1, 3403.15 m (11,165.19 ft), cross-polarized light. (C) Biological shell limestone with ostracod fragments and calcispheres, well LY1, 3833.92 m (12,578.48 ft), PPL. (D) Laminated marl, well NY1, 3430.38 m (11,253.28 ft), PPL. (E) Laminated calcareous mudstone, well NY1, 3488.56 m (11,445.41 ft), PPL. (F) Massive mudstone, well FY1, 3338.35 m (10,952.59 ft), PPL.

The identification of lithofacies is based on the well cores and x-ray data, and the lithofacies of noncored wells are based on the well cuttings and wireline logging data. The lateral continuity and vertical distribution of lithofacies are illustrated by lithofacies cross sections (Figure 6). The Es4s–Es3x shale is laterally continuous. The organic-rich lithofacies increases and silt content decreases from the edge to the center of the basin. The two sections show that the lithofacies have good lateral continuity. The LL-1 is mostly developed in the Es3x-2 interval, and the LDM is predominantly distributed in the Es4s-2 interval.

ORGANIC GEOLOGICAL CHARACTERISTICS

Total Organic Carbon Content and Rock-Eval Pyrolysis

The Es4s–Es3x shale samples from four cored wells have TOC contents in the range of 0.58 to 11.4 wt. %, with an average of 3.17 wt. %. The S1 values range from 0.54 to 22.3 mg/g, with an average of 4.66 mg/g. The S2 values range from 1.99 to 73.51 mg/g, with an average of 19.53 mg/g. The hydrocarbon generation potential (S1 + S2) values range from 2.53 to 87.68 mg/g, with an average of 24.19 mg/g (Figure 7; Table 2). In general, the Es4s–Es3x shale of the Dongying depression has a high content of organic matter, which is closely related to the high paleoproductivity, warm humid climate, and deep-water environment (Zhu et al., 2005; Jia et al., 2013).

Organic-Matter Types

The organic maceral content is dominantly sapropelinite (up to 95%) with subordinate amounts of vitrinite and exinite. The Rock-Eval analysis showed that the hydrogen index (HI) is primarily between 281.34 and 887.1 mg hydrocarbons (HC)/g TOC, with an average of 593.72 mg HC/g TOC. The

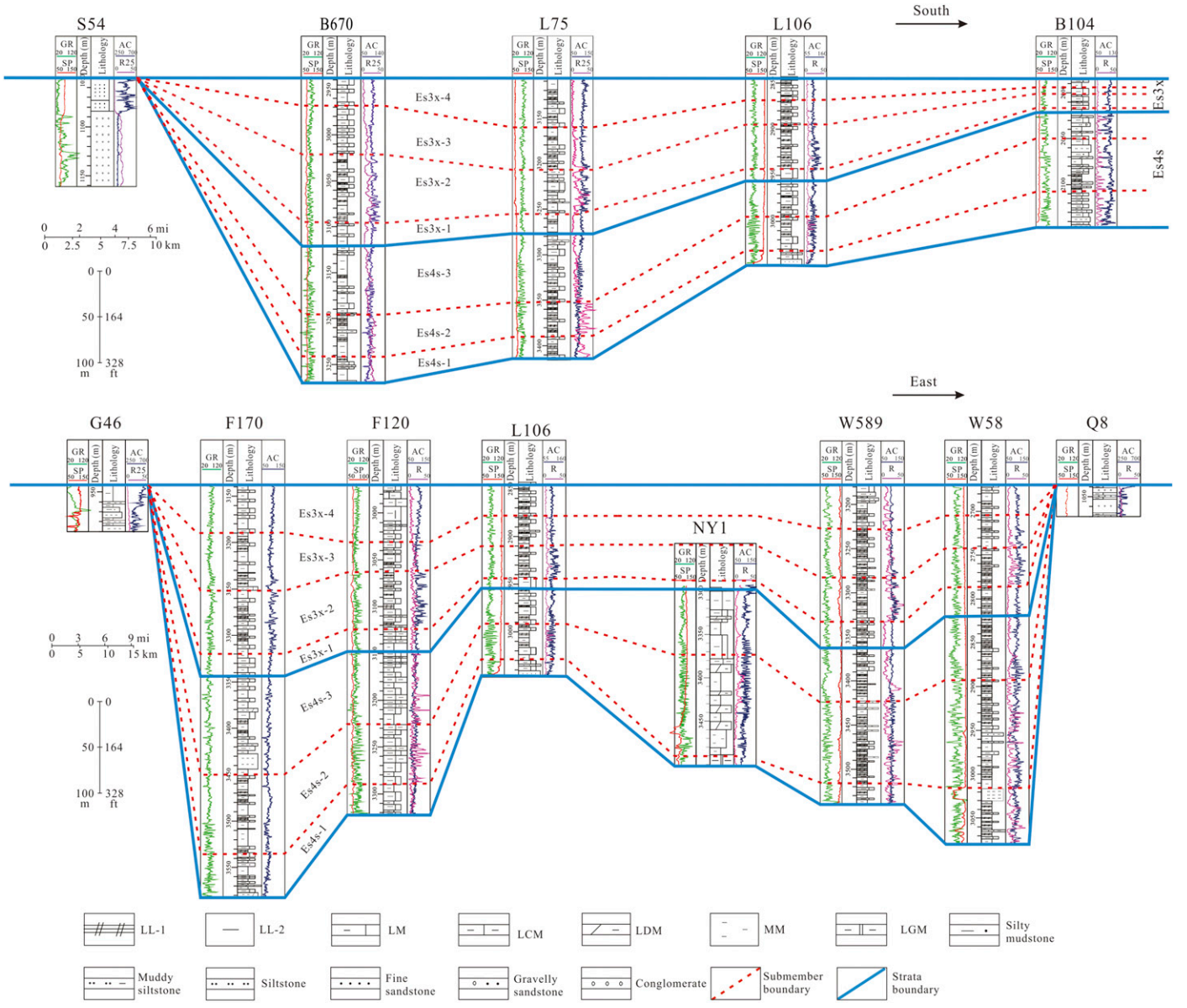

Figure 6. Lithofacies cross sections of Shahejie Formation Es4s–Es3x shale. The datum for this cross section is the top of the Es3x interval. See Figure 1 for the cross section locations. AC = acoustic; GR = natural gamma ray; LCM = laminated calcareous mudstone; LDM = laminated dolomite mudstone; LGM = laminated gypsum mudstone; LL-1 = organic-rich laminated limestone; LL-2 = organic-poor laminated limestone; LM = laminated marl; MM = massive mudstone; R = resistivity; SP = spontaneous potential.

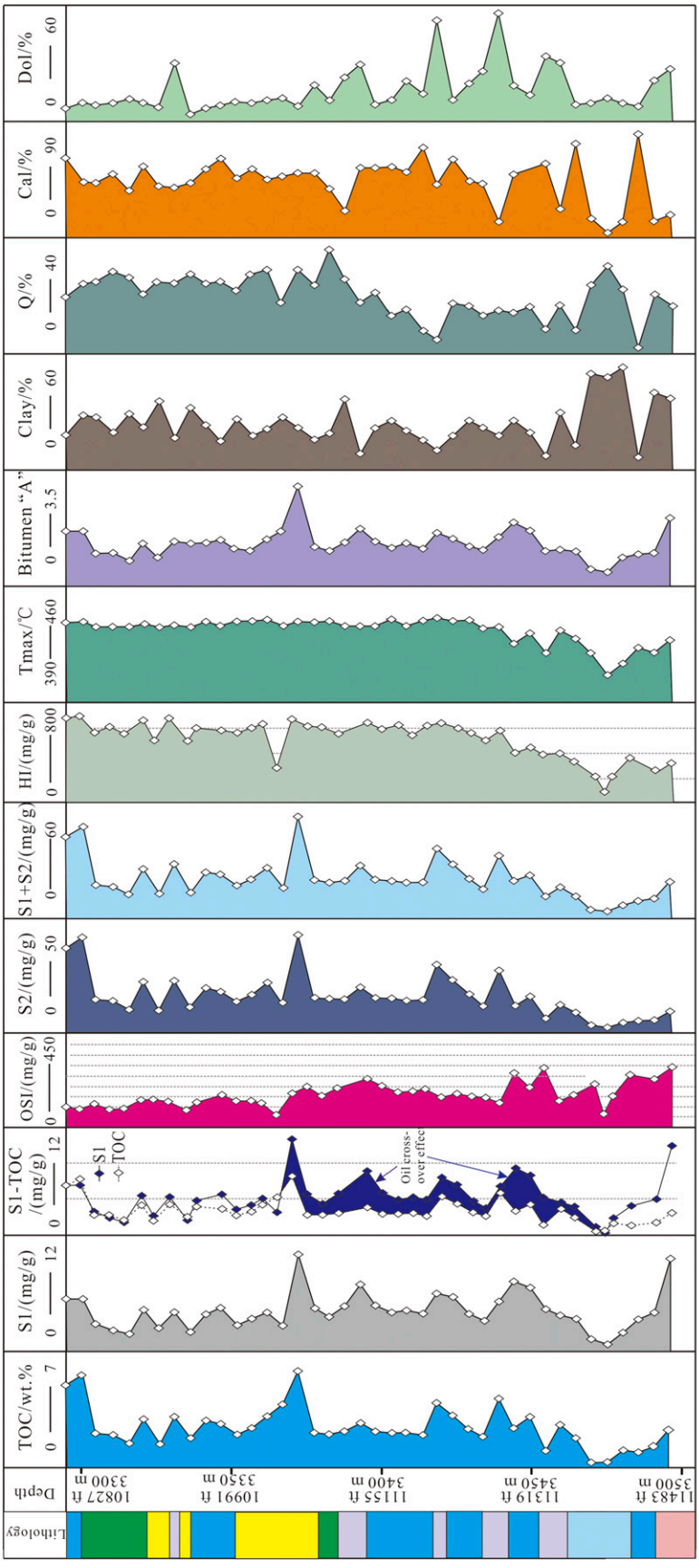

Figure 7. Geochemistry and main mineral composition of the shale in well NY1. Cal = calcite; Dol = dolomite; HI = hydrogen index; LCM = laminated calcareous mudstone; LDM = laminated dolomite mudstone; LGM = laminated gypsum mudstone; LL = laminated limestone; LM = laminated marl; MM = massive mudstone; OSI = oil saturation index; Q = quartz; S1 = free hydrocarbons; S2 = hydrocarbons cracked from kerogen; T_{max} = maximum yield temperature of pyrolysate; TOC = total organic carbon.

T_{max} value ranges from 413°C (775°F) to 450°C (842°F), with an average of 442°C (828°F) (Figure 6; Table 2). The plot of the HI versus the pyrolysis T_{max} is used to classify the maturity and type of organic matter (Figure 8) and shows that the organic matter is predominantly type I to type II kerogen, although a few samples are located in the type III kerogen area, which is consistent with the organic maceral results. The organic matter is predominantly planktonic algae, such as ditch whip algae, coccoliths, and Bohai algae (Wang, 2012).

Thermal Maturity

As mentioned above, the vitrinite is rare in most samples, and the vitrinite values for vitrinite reflectance (R_o) measurement in every sample range from 8 to 15 in this study. Therefore, the plots of HI versus T_{max} and R_o are both used to analyze the thermal maturity synthetically. The R_o ranges from 0.46% to 0.74%. The Es4s–Es3x shale is thermally mature, which is also supported by the T_{max} value between 430°C and 450°C (806°F–842°F) (Figure 8).

PORE CHARACTERISTICS

Interparticle Pores

Interparticle pores identified from FESEM secondary electron images mostly occur within the clay flocculates, fecal pellets, quartz, feldspars, and framboidal pyrite grains. In the Es4s–Es3x shale, some residual interparticle pores persist between compacted grains that underwent burial, for example, the pores at the edge of organic-matter grains, framboidal pyrite grains, and clay minerals (Figure 9A–C), with pore sizes ranging from 0.5 to 2.5 μm. These pores are typically irregular and occur at the grain edge.

Organic-Matter Pores

Round to oval-shaped organic-matter pores exist within densely beaded or "honeycomb" masses within the organic matter. Organic-matter pores range in diameter from 50 to 500 nm, with a small amount up to 1 μm (Figure 9D–F). In the Es4s–Es3x shale, organic pores are common but not well developed.

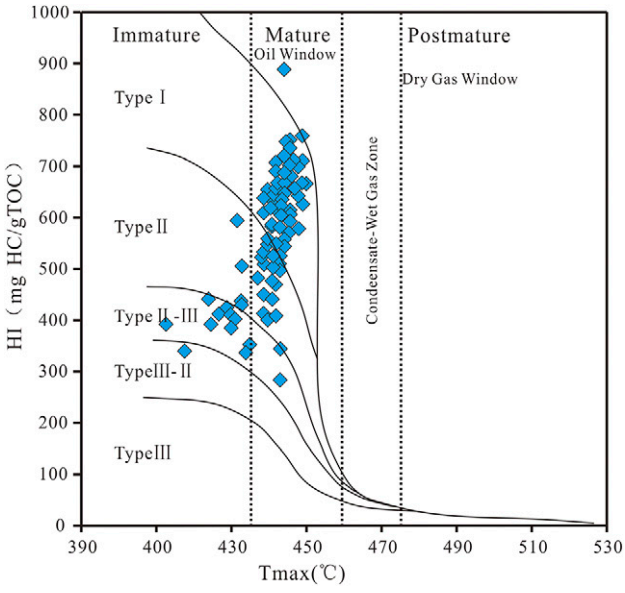

Figure 8. Plot of the hydrogen index (HI) vs. the pyrolysis maximum yield temperature (T_{max}) for the Shahejie Formation Es4s–Es3x shale, showing the kerogen quality and thermal maturity stages. HC = hydrocarbons; TOC = total organic carbon.

The formation of organic-matter pores is related to organic-matter maturation and hydrocarbon generation (Loucks et al., 2012). During the process of organic-matter maturation, organic-matter pores develop in the organic matter and clay minerals rich in organic matter, forming honeycomb pores, which can be observed by FESEM (Figure 9E). Loucks et al. (2012) showed that organic pores were absent or extremely rare in the Barnett Shale at levels of thermal maturity of less than 0.6% R_o. Schieber (2010) noted that the type of organic matter may control the organic pore formation in thermally mature rocks. Studies suggest that type I and type II kerogen may be more prone to the development of organic pores than type III kerogen (Slatt and O'Brien, 2011). In the Es4s–Es3x shale, the TOC content is typically high: up to 8.6 wt. %. The types of organic matter in the Es4s–Es3x shale are type I and type II kerogen. Yet, few organic-matter pores were observed because of the relatively low level of thermal maturity (0.46%–0.74% R_o).

Dissolution Pores

Dissolution pores are observed in calcite and feldspar grains. The dissolution of calcite laminae

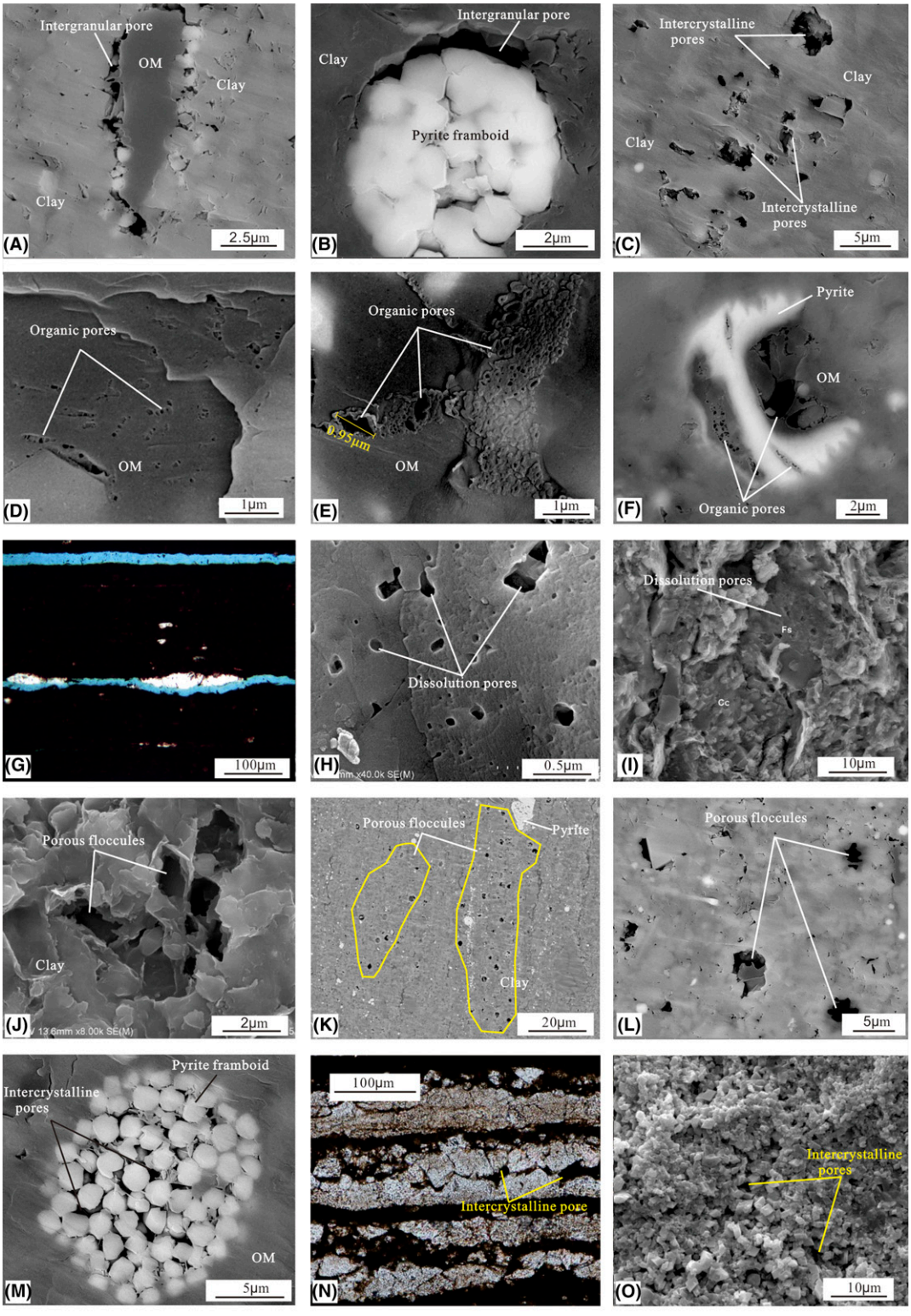
Intergranular pore
OM
Clay
Clay
2.5μm
(A)
Intergranular pore
Clay
Pyrite framboid
2μm
(B)
Intercrystalline pores
Clay
Clay
Intercrystalline pores
5μm
(C)
Organic pores
OM
1μm
(D)
Organic pores
0.95μm
OM
1μm
(E)
Pyrite
OM
Organic pores
2μm
(F)
100μm
(G)
Dissolution pores
0.5μm
(H)
Dissolution pores
Fs
Gc
10μm
(I)
Porous floccules
Clay
2μm
(J)
Porous floccules
Pyrite
Clay
20μm
(K)
Porous floccules
5μm
(L)
Pyrite framboid
Intercrystalline pores
OM
5μm
(M)
100μm
Intercrystalline pore
(N)
Intercrystalline pores
10μm
(O)

forms dissolution pores extending along the lamina edge (Figure 9G). The dissolution pores are elliptical, with pore sizes ranging from 0.1 to 2 μm (Figure 9H, J).

The formation of dissolution pores is thought to be related to organic acids formed during hydrocarbon generation. As mentioned above, the organic matter of Es4s–Es3x shale reaches the mature stage, which will generate abundant organic acidic fluids. These acidic fluids partially dissolve the carbonate and feldspar minerals, resulting in the dissolution pores.

Intracrystalline Pores

Grain-size analyses of modern mud suggest that most particles that are smaller than 10 μm are deposited as floccules (Aplin and Macquaker, 2011). This provides an important mechanism for mud transportation. Floccules are lumps of electrostatically charged clay flakes that sink toward the sea floor in ion-enriched seawater. The floccules can form a "card-house" structure (Bennett et al., 1991). The floccules are porous, which has been confirmed by the freeze-dried flocculated illite in distilled water (O'Brien, 1971), and the porous floccules are available for hydrocarbon storage (Slatt and O'Brien, 2011). The floccule pores are 1–10 μm (Figure 9J) and rich in the clay-rich laminae or shale (Figure 9K). These pores are well connected, which can provide effective pathways for hydrocarbon flow. Some pores contain solid bitumen cement (degraded oil) (Figure 9L), fully demonstrating the effectiveness of these pores.

Deposited in the semideep-lake reducing environment (Zhu et al., 2005; Wang, 2012), the Es4s–Es3x shale contains abundant pyrite, which predominately exists as pyrite framboids. Framboid diameters range from 1 to 10 μm. Large amounts of intracrystalline pores exist among the pyrite crystals (Figure 9M). These pores are 20–50 nm and connective within the pyrite framboids, whereas the pyrite framboids are relatively isolated. These pores are effective for shale gas and oil storage, whereas the oil in these pores is relatively difficult to extract because of the small pore size.

Recrystallization intercrystal pores, including calcite recrystallization intercrystal pores (Figure 9N) and dolomite recrystallization intercrystal pores (Figure 9O), are common in the Es4s–Es3x shale. They are mostly developed in the recrystallized calcite, and a few are developed in the dolomite. Compared with the dolomite recrystallization intercrystal pores, the calcite recrystallization intercrystal pores have larger pore diameters, ranging from tens to hundreds of microns, with bitumen filling in the pores (Figure 9N). The dolomite recrystallization intercrystal pores are typically less than 5 μm.

Figure 9. Representative pore types. (A)–(C) Field-emission–scanning electron microscope (FESEM) images illustrating intergranular and intercrystalline pores with Ar-ion-beam polishing samples (APS). (A) Pores at the edge of organic matter (OM) grain, well NY1, 3436.23 m (11,273.72 ft). (B) Pores at the edge of pyrite framboid with pore sizes of approximately 2 μm, well LY1, 3662.1 m (12,014.76 ft), APS. (C) Pores between clay platelets with pore sizes approximately 1–5 μm, well NY1, 3436.23 m (11,273.72 ft). (D)–(F) The FESEM images illustrating organic pores with APS. (D) Beaded organic pores with pore sizes of approximately 50–500 nm, well N38, 3350 m (10,990.81 ft). (E) Honeycomb organic pores with pore sizes of approximately 20–1000 nm, well LY1, 3662.1 m (12,014.76 ft). (F) Organic pores associated with pyrite, pore sizes of approximately 0.05–2 μm, well LY1, 3805.95 m (12,486.71 ft). (G)–(O) Intraparticle pores. (G) Thin-section image illustrating interpreted interlaminar fractures and possible dissolution pores (blue [in online version]) along the edge of calcite laminae, well N38, 3332.7 m (10,934.06 ft), cross-polarized light. (H) An FESEM image illustrating interpreted dissolution pores in calcite with pore sizes of approximately 0.1–2 μm, well FY1, 3331.55 m (10,930.28 ft), non–Ar-ion-beam polishing sample (NAPS). (I) An FESEM image illustrating interpreted dissolution pores in feldspar grains with pore sizes of approximately 0.5–2 μm, well N38, 3266.11 m (10,715.58 ft), NAPS. (J) An FESEM image illustrating "card-house" porous floccules with the pore sizes of approximately 1–10 μm, well FY1, 3308.4 m (10,854.33 ft), NAPS. (K) An FESEM image illustrating enrichment of multiple floccule pores in the clay laminae with average pore sizes of approximately 5 μm, well NY1, 3436.23 m (11,272.96 ft), APS. (L) An FESEM image showing clay-mineral floccule intercrystalline pores partially filled with bitumen, well NY1, 3436.23 m (11,272.96 ft), APS. (M) An FESEM image illustrating pores between pyrite crystals in the framboid with the pore sizes of approximately 20–50 nm, well N38, 3297.7 m (10,819.25 ft), APS. (N) Thin section illustrating interpreted pores in recrystallized calcite with the pore sizes of approximately 5–50 μm, well FY1, 3419.6 m (11,219.16 ft), plane-polarized light. (O) An FESEM image illustrating intercrystalline pores in recrystallized dolomite with pore sizes of approximately 0.5–5 μm, well NY1, 3460.53 m (11,353.44 ft), NAPS. Cc = calcite; Fs = feldspar.

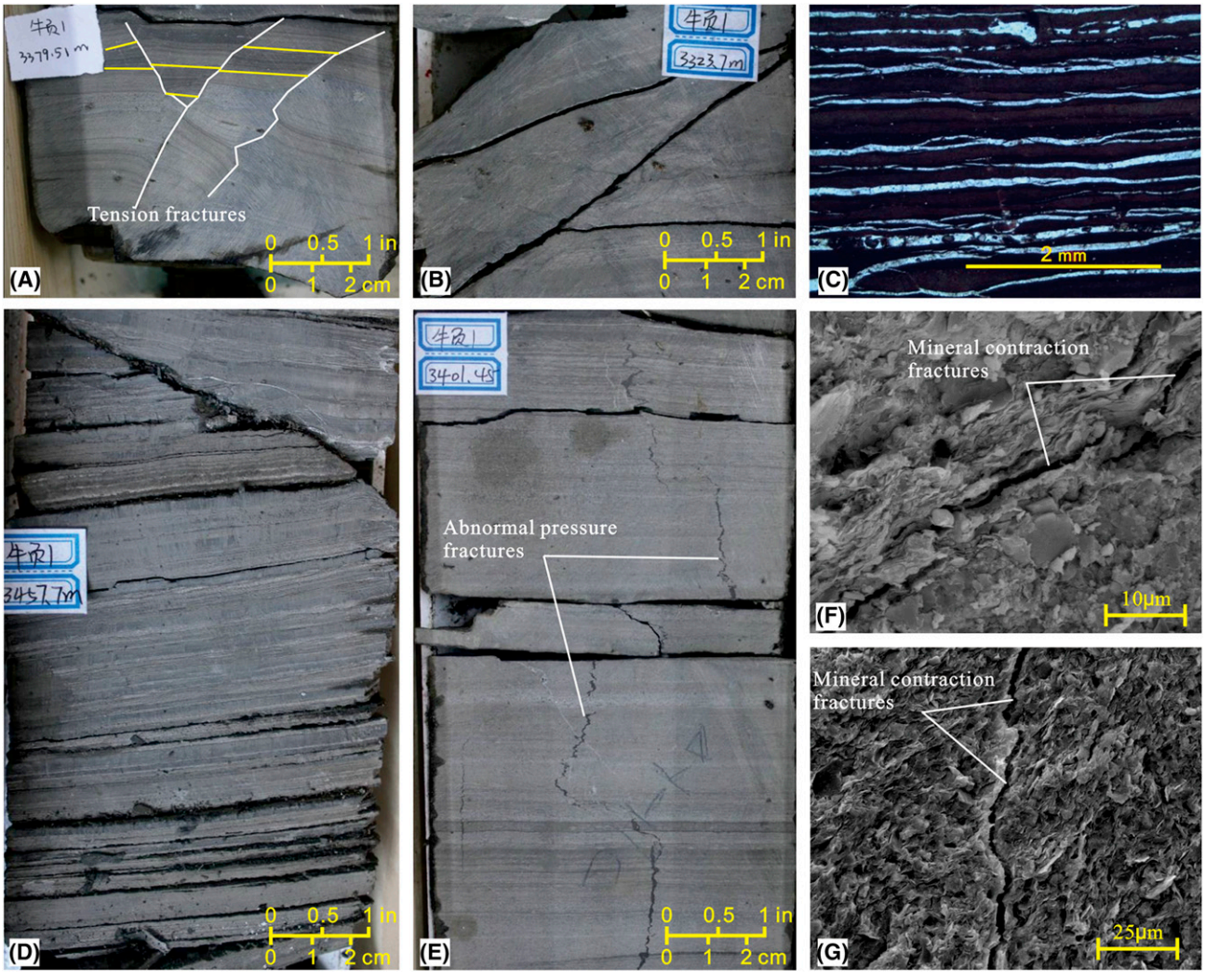

Figure 10. Fracture characteristics. (A) Multiple sets of tension fractures (microfaults) exhibiting offset laminae of 2–10 mm, well NY1, 3379.51 m (11,087.63 ft). (B) Low-angle shear fractures with smooth and straight fracture surfaces, well NY1, 3323.7 m (10,904.53 ft). (C) Interlaminar fractures along laminae, well NY1, 3410.46 m (11,189.17 ft). (D) Well-developed interlaminar fractures in the shale, well NY1, 3457.7 m (11,344.16 ft). (E) Vertical stylolites interpreted as expulsion fractures, partially filled with bitumen, well NY1, 3401.45 m (11,159.61 ft). (F) Field-emission–scanning electron microscope (FESEM) image illustrating mineral-contraction fractures with 1–4 μm widths and 5–20 μm lengths, well NY1, 3301.16 m (10,830.58 ft), non–Ar-ion-beam polishing sample (NAPS). (G) An FESEM image illustrating mineral-contraction fractures with 0.5–2 μm widths and 10–20 μm lengths, well NY1, 3474.55 m (11,399.44 ft), NAPS.

FRACTURE CHARACTERISTICS

Tectonic Fractures

The observation of well cores shows that the fracture surface is straight, laminae are typically faulted, and some fractures are partially or completely filled with calcite (Figure 10A, B). These fractures extend 2–20 cm (0.8–8 in.), with the fractures having openings of 50–200 μm. Tectonic fractures are abundant in the Es4s–Es3x shale and greatly contribute to reservoir permeability in the area. The fracture network formed because of the tectonic stress. The high brittle-mineral content is conducive to the development of tectonic fractures.

Interlaminar Fractures

Interlaminar fractures are characterized as long and continuous (Figure 10C, D), with fractures having openings of 50–200 μm. These fractures develop along the laminae and between different laminae, such as the calcite laminae, clay-rich laminae, and silt-rich

laminae. The fractures can be generated because of differences in the mechanical properties of different laminae. The interlaminar fractures are well developed in laminated shale and can be an excellent lateral migration channel as well as important storage space for shale oil and gas.

Abnormal-Pressure Fractures

Observed in well cores, the fracture surfaces are short and typically irregular. These fractures extend subvertically through undisturbed laminae (Figure 10E). The fractures typically extend 2–10 cm (0.8–4 in.), with fractures opening 50–200 μm. These fractures are abundant in organic-rich lithofacies and nearly perpendicular to the laminae. The fractures are irregular, bifurcated, and filled with bitumen, suggesting that they are nontectonic fractures and act as the pathway for hydrocarbon expulsion. The formation of these fractures may be related to the local abnormal pressure generated during the evolution of organic matter (Ding et al., 2012; Jiu et al., 2013). In the closed shale system, the hydrocarbon generation can create sufficient pressure to exceed the fracture threshold of the rock fabric (Jarvie et al., 2007).

Mineral-Contraction Fractures

The fractures are 5–50 μm in length and 0.5–5 μm in width. Mineral-contraction fracture commonly occurs in the clay-rich laminae. The generation of these microfractures is related to the contraction of clay minerals. In the Es4s–Es3x shale, the clay minerals are illite and illite–montmorillonite mixed layers. The dehydration of clay minerals and the hydrocarbon expulsion of organic matter lead to the generation of many microfractures in the clay laminae during the diagenesis process (Aplin and Macquaker, 2011), both of which can be valid reservoir space in shale (Figure 10F, G).

DISCUSSION

Impact of Organic Matter on Reservoir Properties

Organic-matter pores in shale gas reservoirs are widely reported (Slatt and O'Brien, 2011; Loucks et al., 2012; Liang et al., 2016); however, whether such porosity is effective in shale oil reservoirs remains unclear. Although the TOC content typically has a roughly positive correlation with the porosity (Figure 11A), organic pores do not appear in large numbers in the Es4s–Es3x shale based on the FESEM observations after Ar-ion polishing, which means that organic pores likely do not act as the main storage space. How the TOC content controls the characteristics and porosity of a reservoir remains unclear.

Pores other than organic pores are related to trends in organic matter. As noted above, organic acid expelled during the organic-matter evolution may dissolve carbonate minerals and feldspar, generating dissolution pores (Figure 9H). Meanwhile, organic-matter evolution is prone to cause recrystallization, accompanied by large intercrystal pores, which commonly occur in the recrystallization calcite and dolomite. Zones with a higher TOC content are

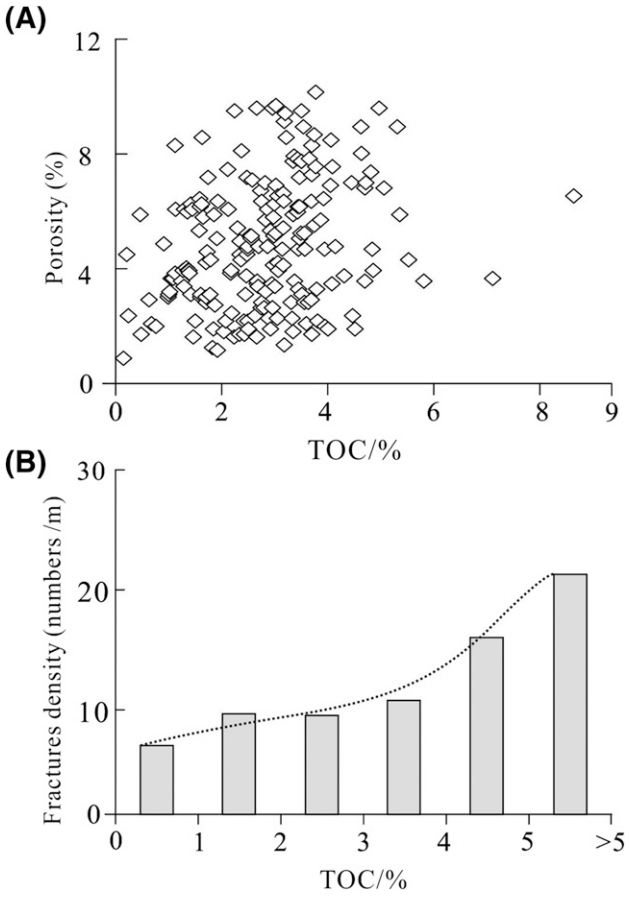

Figure 11. Relationship between (A) porosity, (B) fracture density, and total organic carbon (TOC) content.

thought to generate more organic acid, causing more micritic calcite to recrystallize and grow into larger crystals. The dissolution and recrystallization caused by the hydrocarbon generation provide recrystallization intercrystal pores (Figure 9N), dissolution pores, and interlayer storage space, increasing the porosity to a certain extent. Furthermore, the recrystallization of calcite causes changes in the mechanical properties of rocks and increases the brittleness of the rock (Li, 2013), which is beneficial for shale reservoir fracturing.

Organic matter in shale reservoirs also impacts fracture development. Statistics show that fracture development is closely related to the TOC content, and the fracture density increases exponentially with TOC content (Figure 11B). This correlation occurs because the carbon left after organic-matter expulsion increases the brittleness of shale and easily generates factures in the external force.

Hydrocarbon Generation and Reservoir Brittleness

The Es4s–Es3x shale of the Dongying depression is predominantly type I kerogen, which is the type of organic matter most advantageous for hydrocarbon generation potential (Slatt and O'Brien, 2011; Loucks et al., 2012). This shale is thermally mature ($0.46\% < R_o < 0.74\%$) and has entered the oil window. An abundance of organic matter provides the necessary material basis for the enrichment of shale oil. For shale reservoirs, the hydrocarbons are produced in situ (Jarvie et al., 2007; Curtis et al., 2012;

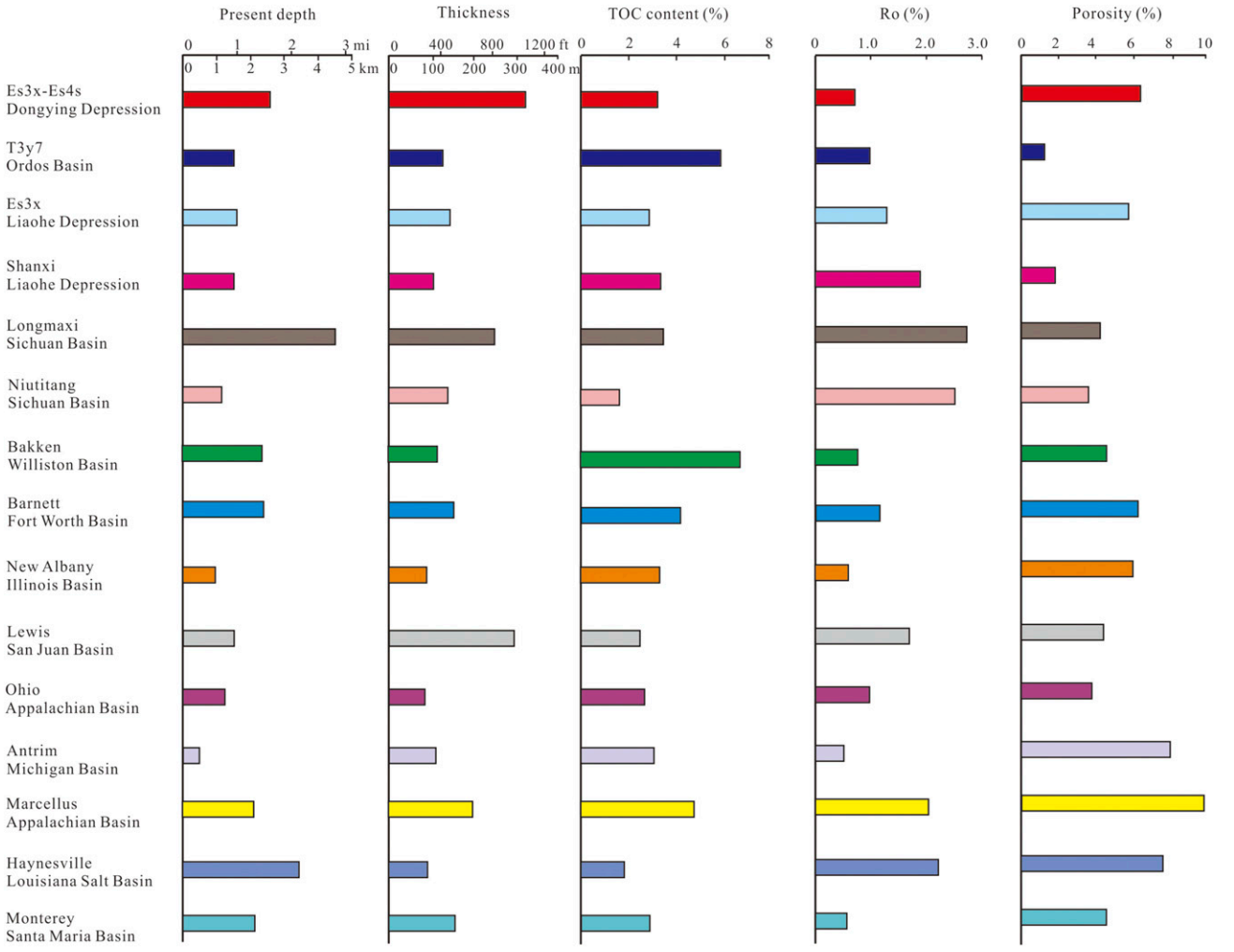

Figure 12. Comparison of Shahejie Formation Es4s–Es3x lacustrine shale with other shales in China and the United States (data obtained from the references shown in Table 5). R_o = vitrinite reflectance; TOC = total organic carbon.

Table 5. Major Shale Reservoir Comparison

Shale	Basin	Present Depth (m [ft])	Thickness (m [ft])	TOC Content (wt. %)	R_o (%)	Porosity (%)	Gas Content (m^3/t [ft^3/t])	Pressure Coefficient	References
Bakken	Williston	2000–3200 (6562–10,499)	30–180 (98–591)	4–15	0.8	4–6	nd	1.35–1.58	Kuhn et al. (2012); Nie et al. (2016)
Barnett	Fort Worth	1981–2591 (6499–8501)	30–240 (98–787)	2–8	1.0–1.3	2–10	8.5–10 (300.2–353.1)	0.99–1.27	Montgomery et al. (2005); Hill et al. (2007); Rodriguez and Philp (2010)
New Albany	Illinois	150–1500 (492–4921)	15–120 (49–394)	1–25	0.4–0.8	5–12	1.1–2.3 (38.8–81.2)	1.15–1.4	Anna et al. (2008); Dong et al. (2011)
Lewis	San Juan	910–1850 (2986–6070)	150–400 (492–1312)	2.4	1.6–1.88	4–6	0.4–1.3 (14.1–45.9)	1.25–1.33	Curtis (2002); Jarvie (2012)
Ohio	Appalachian	1200 (3937)	50–100 (164–328)	1–12	0.4–1.3	3–6	2.2 (77.7)	1.1–1.6	Li et al. (2009); Dong et al. (2011)
Antrim	Michigan	120–730 (394–2395)	30–180 (98–591)	1–18	0.4–0.6	9	1.1–2.8 (38.8–98.9)	nd	Curtis (2002); Anna et al. (2008); Meng and Hou (2012)
Marcellus	Appalachian	475–2591 (1558–8501)	20–300 (66–984)	3–12	1.5–3	10	1.7–2.8 (60–98.9)	nd	Milici and Swezey (2006); Rowan et al. (2015);
Haynesville	Louisiana Salt	3048–4115 (10,000–13,501)	50–100 (164–328)	0.5–4	2.2–3	8–9	2.8–9.35 (98.9–330.2)	nd	Kaiser and Yu (2011); Li et al. (2015)
Monterey	Santa Maria	1000–3700 (3281–12,139)	80–200 (263–656)	1.5–3.5	0.65	nd	nd	nd	Jarvie (2012); Yang et al. (2015)
Longmaxi	Sichuan	600–4500 (1969–14,764)	60–380 (197–1247)	1–9.6	1.3–2.2	3–11	nd	nd	Pu et al. (2010); Liu et al. (2011); Liang et al. (2014)
Niutitang	Sichuan	800–5000 (2625–16,404)	20–315 (66–1034)	0.85–5.8	1.28–5.2	nd	nd	nd	Huang et al. (2012); Han et al. (2013)
Shanxi Formation	Liaohe depression	1800–4500 (5906–14,764)	40–160 (131–525)	0.94–23.2	0.56–2.9	3–8	nd	nd	Yang et al. (2015); Nie et al. (2016)
Es3x	Liaohe depression	2500–4500 (8202–14,764)	60–280 (197–919)	0.8–7.8	0.6–0.8	2–11.4	nd	0.93–1.02	Wu et al. (2013); Zou et al. (2013)
T3y7	Ordos	600–2000 (1969–6562)	100–140 (328–459)	6–22	0.85–1.15	nd	nd	nd	Bai et al. (2009); Yang et al. (2015)
Es4s–Es3x	Dongying depression	2200–4000 (7218–13,123)	50–400 (164–1312)	1.5–11.4	0.6–0.89	2–12	nd	1.3–1.7	Liu et al. (2012); Zhang et al. (2014)

Abbreviations: Es = Shahejie Formation; nd = no data available; R_o = vitrinite reflectance; TOC = total organic carbon.

Zou et al., 2013). Therefore, the effective thickness of the shale becomes another important indicator of shale oil enrichment. The Es4s–Es3x shale was deposited in a relatively stable deep-water environment, characterized by a wide horizontal distribution and relatively continuous vertical thickness. The thickness of organic-rich shale (TOC > 2 wt. %) is greater than 50 m (164 ft), and the area can reach 1024 km^2 (395 mi^2) (Wang et al., 2013). The source-rock quality, thermal maturity, and effective thickness of organic-rich shales are advantageous for hydrocarbon generation.

Studies reveal that rock brittleness is related to the mineral composition and increases with an abundance of brittle minerals (Curtis, 2002; Liang et al., 2014). Tectonic processes, diagenesis, and artificial fracturing can form large quantities of different scales of fractures in brittle strata, which may interconnect isolated pores, thus creating migration pathways within the shale (Gale et al., 2007; Tang et al., 2012; Jiu et al., 2013; Ferrill et al., 2014). As noted above, the content of brittle minerals in the Es4s–Es3x shale ranges from 51 to 87 wt. %, with an average of 72 wt. %. The relatively high content of brittle minerals facilitates artificial fracturing during the exploitation of shale oil and gas. With the increase of compaction and maturity, unstable clay minerals gradually transform into more stable clay minerals (such as illite), which make shale dense. In addition, some microquartz originated from the desiliconization of clay minerals, increasing the brittle-mineral content and the quartz/quartz + calcite + clay ratio, which is closely related to the brittleness. Therefore, the brittleness of shale is also impacted by the diagenesis (Jarvie et al., 2007; Li, 2013).

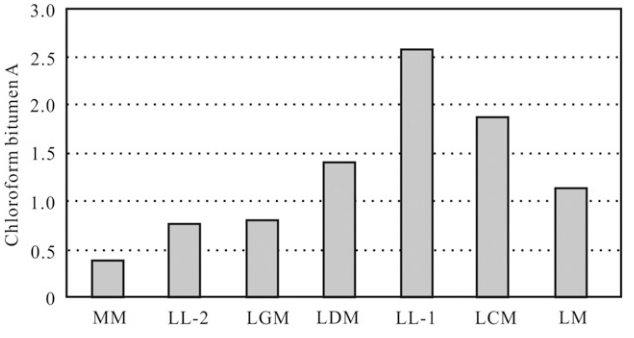

Figure 13. Chloroform bitumen "A" of different lithofacies. LCM = laminated calcareous mudstone; LDM = laminated dolomite mudstone; LGM = laminated gypsum mudstone; LL-1 = organic-rich laminated limestone; LL-2 = organic-poor laminated limestone; LM = laminated marl; MM = massive mudstone.

The Es4s–Es3x shale was deposited in the semideep and deep lake environment and formed at the basin expansion phase. The depositional environment and process of the lacustrine carbonate-rich Es4s–Es3x shale are different from the marine-continental transitional and marine shales, such as the Shanxi Formation in the Liaohe depression, the Yanchang Formation in the Ordos Basin and Bohai Bay Basin, and the Cambrian Niutitang and Silurian Longmaxi shales in Sichuan Basin, South China (Bai et al., 2009; Hao et al., 2013; Wang et al., 2014; Nie et al., 2016). Comparative analysis demonstrated that the TOC content and carbonate minerals of lacustrine shale are much higher compared with the marine and marine-continental transitional shale (Figure 12; Table 5).

In addition, compared with some major shales in the United States, the Es4s–Es3x shale is characterized by deep burial depth, low thermal maturity, high carbonate content, and low quartz content (Figure 12; Table 5). These differences affect the types of pores developed in the Es4s–Es3x shale as compared with most marine shales (Hill et al., 2007; Jarvie et al., 2007; Wang et al., 2014; Yang et al., 2015). As mentioned above, the organic-matter pores are the key storage space in the marine gas shales but not in the Es4s–Es3x shale. The carbonate recrystallization intercrystal pores and dissolution pores act as the main matrix pores in the Es4s–Es3x shale. The differences in lithology, pore type, and thermal maturity will bring new challenges of lacustrine-shale oil and gas exploration and exploitation (Wu et al., 2013; Zou et al., 2013).

The "Sweet Spot"

For shale reservoir exploration, achieving the sweet spot (the favorable lithofacies) is critical. In contrast to the various lithofacies noted above, the LL-1 contains abundant reservoir space, such as recrystallization intercrystal pores, interlaminar fractures, and organic pores (Table 3); LL-1 has high TOC content (average of 4.68 wt. %), chloroform bitumen A content (average of 2.6 wt. %, Figure 13), and brittle-mineral content (average of 70 wt. %). For

high-quality shale reservoirs, abundant reservoir space and good connectivity, high organic abundance and hydrocarbon potential, high brittleness, and other factors are indispensable (Montgomery et al., 2005; Hill et al., 2007; Jarvie et al., 2007).

The cumulative thickness of LL-1 is 36 m (118 ft) in the Es4s–Es3x shale of well NY1, with single-bed thickness of 2–6 m (7–20 ft). In addition, LL-1 is associated with other lithofacies with relatively good reservoir properties and hydrocarbon potential, such as laminated calcareous mudstone (LCM) and laminated marl (LM). The Es3x-2 in which the LL-1 is well developed is the most favorable exploration interval (Figure 6).

CONCLUSIONS

Lacustrine black shale is well developed in the Dongying depression and primarily developed as five lithofacies: laminated limestone, LM, LCM, laminated gypsum mudstone, and MM. Evaluation of the organic geochemical and petrographic data shows that the calcareous organic-rich lithofacies possess good potential for hydrocarbon generation. Reservoir spaces include pores and fractures: interparticle pores, organic-matter pores, dissolution pores, intracrystalline pores, interlaminar fractures, tectonic fractures, and abnormal-pressure fractures. Organic-matter pores are the key storage space in marine gas shales but are poorly developed in the Es4s–Es3x shale because of low thermal maturity. The recrystallization intercrystal pores and dissolution pores associated with the organic-matter evolution are the main form of matrix pore storage. The high organic-matter content and effective thickness of the organic-rich shales are the basis for the hydrocarbon generation and accumulation. The relatively high brittle-mineral content (up to 87%) facilitates both natural and artificial fractures that are believed to be critical for exploitation of the shale oil. The Es4s–Es3x shale is characterized by deep burial depth, low thermal maturity, high carbonate content, and low quartz content. Understanding these differences of marine and lacustrine shales helps with analyzing the lacustrine-shale oil exploration potential and favorable exploration target selection.

REFERENCES CITED

Abouelresh, M. O., and R. M. Slatt, 2012, Lithofacies and sequence stratigraphy of the Barnett Shale in east-central Fort Worth Basin, Texas: AAPG Bulletin, v. 96, no. 1, p. 1–22, doi:10.1306/04261110116.

Anna, M. M., M. W. Lynn, and J. C. Mclntosh, 2008, Identification of microbial and thermogenic gas components from Upper Devonian black shale cores, Illinois and Michigan basins: AAPG Bulletin, v. 92, no. 3, p. 327–339, doi:10.1306/10180706037.

Aplin, A. C., and J. H. S. Macquaker, 2011, Mudstone diversity: Origin and implications for source, seal, and reservoir properties in petroleum systems: AAPG Bulletin, v. 95, no. 12, p. 2031–2059, doi:10.1306/03281110162.

Bai, Y. L., L. Ma, W. J. Wu, and Y. H. Ma, 2009, Geological characteristics and resource potential of oil shale in Ordos Basin: Geology in China, v. 36, no. 5, p. 1123–1137.

Barker, C., 1974, Pyrolysis techniques for source-rock evaluation: AAPG Bulletin, v. 58, no. 11, p. 2349–2361.

Bennett, R. H., N. R. O'Brien, and M. H. Hulbert, 1991, Determinants of clay and shale microfabric signatures: Processes and mechanisms, *in* R. H. Bennet, W. R. Bryant, M. H. Hulbert, W. A. Chiou, R. W. Faas, J. Kasprowicz and H. Li, et al., eds., Microstructure of fine grained sediments: From mud to shale: New York, Springer, p. 5–32, doi:10.1007/978-1-4612-4428-8_2.

Burton, D., K. Woolf, and B. Sullivan, 2014, Lacustrine depositional environments in the Green River Formation, Uinta Basin: Expression in outcrop and wireline logs: AAPG Bulletin, v. 98, no. 9, p. 1699–1715, doi:10.1306/03201413187.

Charles, M. J., and M. S. Simmons, 1986, Methods for the determination of carbon in soils and sediments. A review: Analyst, v. 111, no. 4, p. 385–390, doi:10.1039/AN9861100385.

Chen, X., M. Wang, Y. X. Yan, X. W. Zhang, X. Luo, and Y. H. Zhang, 2011, Accumulation conditions for continental shale oil and gas in the Biyang Depression: Oil & Gas Geology, v. 32, no. 4, p. 568–577.

Curtis, J. B., 2002, Fractured shale-gas systems: AAPG Bulletin, v. 86, no. 11, p. 1921–1938.

Curtis, M. E., C. H. Sondergeld, R. J. Ambrose, and C. S. Rai, 2012, Microstructural investigation of gas shales in two and three dimensions using nanometer-scale resolution imaging: AAPG Bulletin, v. 96, no. 4, p. 665–677, doi:10.1306/08151110188.

Ding, W. L., C. Li, C. Y. Li, C. C. Xu, K. Jiu, and W. T. Zeng, 2012, Dominant factor of fracture development in shale and its relationship to gas accumulation: Earth Science Frontiers, v. 19, no. 2, p. 212–220.

Dong, D. Z., C. N. Zou, J. Z. Li, S. J. Wang, X. J. Li, Y. M. Wang, D. H. Li, and J. L. Huang, 2011, Resource potential, exploration and development prospect of shale gas in the whole world: Geological Bulletin of China, v. 30, no. 2/3, p. 324–336.

El Attar, A., and M. J. Pranter, 2016, Regional stratigraphy, elemental chemostratigraphy, and organic richness of

the Niobrara Member of the Mancos Shale, Piceance Basin, Colorado: AAPG Bulletin, v. 100, no. 3, p. 345–377, doi:10.1306/12071514127.
Espitalie, J., G. Deroo, and F. Marquis, 1986, Rock-Eval pyrolysis and its applications: Revue de l'Institut Francais du Petrole, v. 41, p. 73–89.
Fairbanks, M. D., S. C. Ruppel, and H. Rowe, 2016, High-resolution stratigraphy and facies architecture of the Upper Cretaceous (Cenomanian–Turonian) Eagle Ford Group, Central Texas: AAPG Bulletin, v. 100, no. 3, p. 379–403, doi:10.1306/12071514187.
Ferrill, D. A., A. P. Morris, P. H. Hennings, and D. E. Haddad, 2014, Faulting and fracturing in shale and self-sourced reservoirs: Introduction: AAPG Bulletin, v. 98, no. 11, p. 2161–2164, doi:10.1306/intro073014.
Gale, J. F. W., R. M. Reed, and J. Holder, 2007, Natural fractures in the Barnett shale and their importance for hydraulic fracture treatments: AAPG Bulletin, v. 91, no. 4, p. 603–622, doi:10.1306/11010606061.
Guo, X. W., K. Y. Liu, C. Z. Jia, Y. Song, M. J. Zhao, and X. S. Lu, 2016, Effects of early petroleum charge and overpressure on reservoir porosity preservation in the giant Kela-2 gas field, Kuqa depression, Tarim Basin, northwest China: AAPG Bulletin, v. 100, no. 2, p. 191–212, doi:10.1306/11181514223.
Han, S. B., J. C. Zhang, Y. X. Li, B. Horsfield, X. Tang, W. L. Jiang, and Q. Chen, 2013, Evaluation of lower Cambrian shale in northern Guizhou Province, South China: Implications for shale gas potential: Energy & Fuels, v. 27, no. 6, p. 2933–2941, doi:10.1021/ef400141m.
Hao, F., H. Zou, and Y. Lu, 2013, Mechanisms of shale gas storage: Implications for shale gas exploration in China: AAPG Bulletin, v. 97, no. 8, p. 1325–1346, doi:10.1306/02141312091.
He, S., G. Q. Song, Y. S. Wang, X. F. Hao, B. J. Wang, N. Li, and S. Y. Luo, 2012, Distribution and major control factors of the present-day large scale overpressured system in Dongying Depression: Earth Science-Journal of China University of Geosciences, v. 37, no. 5, p. 1029–1042.
Hill, R. J., D. M. Jarvie, J. Zumberge, M. Henry, and R. M. Pollastro, 2007, Oil and gas geochemistry and petroleum systems of the Fort Worth Basin: AAPG Bulletin, v. 91, no. 4, p. 445–473, doi:10.1306/11030606014.
Huang, J. L., C. N. Zou, J. Z. Li, D. Z. Dong, S. J. Wang, S. Q. Wang, and K. M. Cheng, 2012, Shale gas generation and potential of the Lower Cambrian Qiongzhusi Formation in Southern Sichuan Basin, China: Petroleum Exploration and Development, v. 39, p. 75–81, doi:10.1016/S1876-3804(12)60017-2.
Jarvie, D. M., 2012, Shale resource systems for oil and gas: Part 2—Shale-oil resource systems, *in* J. A. Breyer, ed., Shale reservoir—Giant resources for the 21st century: AAPG Memoir 97, p. 89–119.
Jarvie, D. M., R. J. Hill, T. E. Ruble, and R. M. Pollastro, 2007, Unconventional shale-gas systems: The Mississippian Barnett Shale of north-central Texas as one model for thermogenic shale-gas assessment: AAPG Bulletin, v. 91, no. 4, p. 475–499, doi:10.1306/12190606068.
Jia, J. L., A. Bechtel, Z. J. Liu, S. A. I. Strobl, P. Sun, and R. F. Sachsenhofer, 2013, Oil shale formation in the Upper Cretaceous Nenjiang Formation of the Songliao Basin (NE China). Implications from organic and inorganic geochemical analyses: International Journal of Coal Geology, v. 113, no. 7, p. 11–26, doi:10.1016/j.coal.2013.03.004.
Jiang, X. F., 2011, Main controlling factors of lacustrine carbonate deposition in Jiyang Depression: Petroleum Geology and Recovery Efficiency, v. 18, no. 6, p. 24–30.
Jiang, Z. X., C. Liang, J. Wu, J. G. Zhang, W. Z. Zhang, Y. S. Wang, H. M. Liu, and X. , 2013, Aspects of sedimentological studies on oil/gas bearing fine-grained sedimentary rocks: Acta Petrolei Sinica, v. 34, no. 6, p. 1–9.
Jiu, K., W. L. Ding, W. H. Huang, Y. Q. Zhang, S. Zhao, and L. J. Hu, 2013, Fractures of lacustrine shale reservoirs, the Zhanhua Depression in the Bohai Bay Basin, eastern China: Marine and Petroleum Geology, v. 48, p. 113–123, doi:10.1016/j.marpetgeo.2013.08.009.
Kaiser, M. J., and Y. Yu, 2011, Haynesville shale well performance and development potential: Natural Resources Research, v. 20, no. 4, p. 217–229, doi:10.1007/s11053-011-9147-z.
Kuhn, P. P., R. di Primio, R. Hill, J. R. Lawrence, and B. Horsfield, 2012, Three-dimensional modeling study of the low-permeability petroleum system of the Bakken Formation: AAPG Bulletin, v. 96, no. 10, p. 1867–1897, doi:10.1306/03261211063.
Li, J. Y., 2013, Analysis on mineral components and frangibility of shales in Dongying Depression: Acta Sedimentologica Sinica, v. 31, no. 4, p. 616–620.
Li, X. J., Z. G. Lu, D. Z. Dong, and K. M. Cheng, 2009, Geologic controls on accumulation of shale gas in North America: Natural Gas Industry, v. 29, no. 5, p. 27–32.
Li, Z. M., X. Q. Rui, M. W. Li, T. T. Cao, E. S. Xu, G. L. Tao, and Q. G. Jiang, 2015, Characteristics of typical hybrid shale-oil system in north American and its implications: Journal of Jilin University (Earth Science Edition), v. 45, no. 4, p. 1060–1072.
Li, Z., Y. Zou, X. Xu, J. Sun, M. Li, and P. A. Peng, 2016, Adsorption of mudstone source rock for shale oil-experiments, model and a case study: Organic Geochemistry, v. 92, p. 55–62, doi:10.1016/j.orggeochem.2015.12.009.
Liang, C., Z. X. Jiang, Y. C. Cao, M. H. Wu, L. Guo, and C. M. Zhang, 2016, Deep-water depositional mechanisms and significance for unconventional hydrocarbon exploration: A case study from the lower Silurian Longmaxi shale in the southeastern Sichuan Basin: AAPG Bulletin, v. 100, no. 5, p. 773–794, doi:10.1306/02031615002.
Liang, C., Z. X. Jiang, C. M. Zhang, L. Guo, Y. T. Yang, and J. Li, 2014, The shale characteristics and shale gas exploration prospects of the Lower Silurian Longmaxi shale, Sichuan Basin, South China: Journal of Natural Gas Science and Engineering, v. 21, p. 636–648, doi:10.1016/j.jngse.2014.09.034.
Liu, H., Y. L. Jiang, G. Q. Song, D. M. Cai, and H. Q. Xu, 2012, Pressure evolution and gas accumulation of the fourth member of the Shahejie Formation in Dongying Depression, Bohai Bay Basin: Acta Sedimentologica Sinica, v. 30, no. 1, p. 197–204.

Liu, S. G., W. X. Ma, J. Luba, W. M. Huang, H. L. Zeng, and C. J. Zhang, 2011, Characteristics of the shale gas reservoir rocks in the Lower Silurian Longmaxi Formation, East Sichuan basin, China: Yanshi Xuebao, v. 27, p. 2239–2252.

Liu, C. L., X. X. Shu, and Z. W. Liu, 2001, Microcharacteristics of Paleogene lacustrine petroleum source rocks in Jiyang Depression: Acta Sedimentologica Sinica, v. 19, no. 2, p. 293–297.

Liu, Q., L. Y. Zhang, Z. M. Shen, X. X. Kong, and Z. Li, 2004, Evolution of lake basin types and occurrence of hydrocarbon source rocks in Dongying Depression: Acta Petrolei Sinica, v. 25, no. 4, p. 42–45.

Loucks, R. G., R. M. Reed, S. C. Ruppel, and U. Hammes, 2012, Spectrum of pore types and networks in mudrocks and a descriptive classification for matrix-related mudrock pores: AAPG Bulletin, v. 96, no. 6, p. 1071–1098, doi:10.1306/08171111061.

Loucks, R. G., and S. C. Ruppel, 2007, Mississippian Barnett mudstone: Lithofacies and depositional setting of a deep-water mudstone-gas succession in the Fort Worth basin, Texas: AAPG Bulletin, v. 91, no. 4, p. 579–601, doi:10.1306/11020606059.

Lu, S. F., W. B. Huang, F. W. Chen, J. J. Li, M. Wang, H. T. Xue, W. M. Wang, and X. Y. Cai, 2012, Classification and evaluation criteria of shale oil and gas resources: Discussion and application: Petroleum Exploration and Development, v. 39, no. 2, p. 268–276, doi:10.1016/S1876-3804(12)60042-1.

Meng, Q. F., and G. T. Hou, 2012, Characteristics and implications of Marcellus shale gas reservoir: Appalachian Basin: China Petroleum Exploration, v. 17, no. 1, p. 65–73.

Milici, R. C., and C. S. Swezey, 2006, Assessment of Appalachian Basin oil and gas resources: Devonian shale-middle and upper Paleozoic total petroleum system: Reston, Virginia, US Geological Survey Open-File Report 2006-1237, 70 p.

Montgomery, S. L., D. M. Jarvie, K. A. Bowker, and R. M. Pollastro, 2005, Mississippian Barnett Shale, Fort Worth basin, north-central Texas: Gas-shale play with multi-trillion cubic foot potential: AAPG Bulletin, v. 89, no. 2, p. 155–175, doi:10.1306/09170404042.

Nie, H. K., P. X. Zhang, R. K. Bian, X. L. Wu, and C. B. Zhai, 2016, Oil accumulation characteristics of China continental shale: Earth Science Frontiers, v. 23, no. 2, p. 55–62.

O'Brien, N. R., 1971, Fabric of kaolinite and illite floccules: Clays and Clay Minerals, v. 19, p. 353–359, doi:10.1346/CCMN.1971.0190603.

Pu, B. L., Y. L. Jiang, Y. Wang, S. J. Bao, and X. J. Liu, 2010, Reservoir-forming conditions and favorable exploration zones of shale gas in Lower Silurian Longmaxi Formation of Sichuan Basin: Acta Petrolei Sinica, v. 31, p. 225–230.

Qiu, N. S., X. G. Su, Z. Y. Li, Z. Q. Liu, and Z. Li, 2006, The Cenozoic tectono-thermal evolution of Jiyang Depression, Bohai Bay basin, East China: Chinese Journal of Geophysics, v. 49, no. 4, p. 1015–1024, doi:10.1002/cjg2.923.

Rodriguez, N. D., and R. P. Philp, 2010, Geochemical characterization of gases from the Mississippian Barnett shale, Fort Worth Basin, Texas: AAPG Bulletin, v. 94, no. 11, p. 1641–1656, doi:10.1306/04061009119.

Rowan, E. L., M. A. Engle, T. F. Kraemer, K. T. Schroeder, R. W. Hammack, and M. W. Doughten, 2015, Geochemical and isotopic evolution of water produced from Middle Devonian Marcellus shale gas wells, Appalachian basin, Pennsylvania: AAPG Bulletin, v. 99, no. 1, p. 181–206, doi:10.1306/07071413146.

Saraji, S., and M. Piri, 2015, The representative sample size in shale oil rocks and nano-scale characterization of transport properties: International Journal of Coal Geology, v. 146, no. 7, p. 42–54, doi:10.1016/j.coal.2015.04.005.

Schenk, C. J., M. E. Brownfield, R. R. Charpentier, T. A. Cook, T. R. Klett, M. A. Kirschbaum, J. K. Pitman, and R. M. Pollastro, 2010, Assessment of undiscovered oil and gas resources of southeast Asia, 2010: Reston, Virginia, US Geological Survey Fact Sheet 2010-3015, 4 p.

Schenk, C. J., R. R. Charpentier, T. R. Klett, M. E. Tennyson, T. J. Mercier, M. E. Brownfield, J. K. Pitman, S. B. Gaswirth, and H. M. Leathers-Miller, 2015, Assessment of shale-oil resources of the Central Sumatra Basin, Indonesia, 2015: Reston, Virginia, US Geological Survey Fact Sheet 2015–3072, 2 p.

Schieber, J., 2010, Common themes in the formation and preservation of porosity in shales and mudstones: Illustrated with examples across the Phanerozoic: SPE Unconventional Gas Conference, Pittsburgh, Pennsylvania, February 23–25, 2010, SPE-132370-MS, 10 p., doi:10.2118/132370-MS.

Sheng, W. B., Y. C. Cao, H. Liu, and Y. Zhang, 2008, Evolutionary characteristics of the Palaeogene basin-controlling boundary fault sand types of basin architectures in the Dongying Depression: Oil & Gas Geology, v. 29, no. 3, p. 290–296.

Slatt, R. M., and N. R. O'Brien, 2011, Pore types in the Barnett and Woodford gas shales: Contribution to understanding gas storage and migration pathways in fine-grained rocks: AAPG Bulletin, v. 95, no. 12, p. 2017–2030, doi:10.1306/03301110145.

Song, G. Q., L. Y. Zhang, S. F. Lu, X. Xu, R. Zhu, M. Wang, and Z. Li, 2013, Resource evaluation method for shale oil and its application: Earth Science Frontiers, v. 20, no. 4, p. 221–228.

Tang, Y., Y. Xing, L. Z. Li, B. H. Zhang, and S. X. Jiang, 2012, Influence factors and evaluation methods of the gas shale fracability: Earth Science Frontiers, v. 19, no. 5, p. 356–363.

Wang, G. M., 2012, Laminae combination and genetic classification of Eogene shale in Jiyang Depression: Journal of Jilin University (Earth Science Edition), v. 42, no. 3, p. 666–680.

Wang, Y. S., Z. Li, J. Q. Gong, J. J. Zhu, Y. Q. Hao, X. F. Hao, and Y. Wang, 2013, Discussion on an evaluation method of shale oil and gas in Jiyang Depression: A case study on Luojia area in Zhanhuasag: Acta Petrolei Sinica, v. 34, no. 1, p. 83–90.

Wang, M., L. Shi, W. G. Wang, A. H. Huang, G. H. Chen, and S. S. Tian, 2014, Comparative study on geochemical characteristics of shale oil between China and U.S.A.: Lithologic Reservoirs, v. 26, no. 3, p. 67–74.

Wu, X. L., B. Gao, X. Ye, R. K. Bian, H. K. Nie, and F. C. Lu, 2013, Shale oil accumulation conditions and exploration potential of faulted basins in the east of China: Oil & Gas Geology, v. 34, no. 4, p. 455–462.

Xue, Y., Z. P. Wu, W. Li, and W. L. Nie, 2013, Cenozoic Basin structure in the Dongying Depression and its control over reservoir: Geotectonica et Metallogenia, v. 37, no. 2, p. 206–212.

Yang, Y. T., C. Liang, J. C. Zhang, Z. X. Jiang, and X. Tang, 2015, A developmental model of lacustrine shale gas genesis: A case from T3y7 shale in the Ordos Basin, China: Journal of Natural Gas Science and Engineering, v. 22, p. 395–405, doi:10.1016/j.jngse.2014.12.014.

Zhang, L. Y., S. Y. Bao, J. Y. Li, Z. Li, R. F. Zhu, and J. G. Zhang, 2014, Movability of lacustrine shale oil: A case study of Dongying Sag, Jiyang Depression, Bohai Bay Basin: Petroleum Exploration and Development, v. 41, no. 6, p. 703–711, doi:10.1016/S1876-3804(14)60084-7.

Zhang, S. W., L. Y. Zhang, S. C. Zhang, Q. Liu, R. F. Zhu, and S. Y. Bao, 2009, Formation of abnormal high pressure and its application in the study of oil-bearing property of lithologic hydrocarbon reservoirs in the Dongying Sag: Chinese Science Bulletin, v. 54, no. 11, p. 1570–1578.

Zhu, G. Y., Q. Jin, S. C. Zhang, J. X. Dai, G. M. Wang, L. Y. Zhang, and J. Li, 2005, Characteristics and origin of deep lake oil shale of the Shahejie Formation of Paleogene in Dongying Depression: Journal of Palaeogeography, v. 7, no. 1, p. 59–69.

Zou, C. N., Z. Yang, and J. W. Cui, 2013, Formation mechanism, geological characteristics and development strategy of nonmarine shale oil in China: Petroleum Exploration and Development, v. 40, no. 1, p. 15–27, doi:10.1016/S1876-3804(13)60002-6.